Representative Volume Element for Modelling the In-Plane Mechanical Behaviour of Paperboard:

Utilizing Microstructure from X-ray Tomography

Master's Dissertation by

Stina Starkenberg & Saga Wennerholm

Preface

This Master Thesis in Mechanical Engineering was conducted between January 2024 and June 2024 at the Division of Solid Mechanics, Lund university, in collaboration with Tetra Pak.

We want to express our gratitude to our Tetra Pak supervisors Eric Borgqvist and Eskil Andresson. Eric, your dedication to this project and expertise in paper physics have been crucial for this project's progress. Eskil, your support and enthusiasm, no matter the topic, are truly inspiring.

We would also like to thank everyone at Tetra Pak who contributed to this project. Special recognition goes to Fredrik Linell for X-ray assistance, Philip Claesson for guidance in programming and Abaqus, and Johan Tryding for material calibration insights. Your help has been of great importance to the progress of this project.

Finally, we would like to thank our supervisor at the Division of Solid Mechanics, Matti Ristinmaa, for your incredible support, guidance, and patience in answering all of our questions.

Thanks to all of our supervisors, we have gained a deeper understanding, knowledge, and most importantly, interest in this subject.

Abstract

The aim of this project is to establish a workflow that transforms CT-scanned images of paperboard into a calibrated Representative Volume Element (RVE). A RVE is defined as the smallest volume that accurately captures the macroscopic behavior of the material.

First, CT-scanned images are converted into a finite element model that represents the microstructure of the paperboard. Secondly, a discrete field of fiber orientations are established by using Structure Tensor analysis. Thereafter, transverse isotropic material parameters of fibers are calibrated using the Hill yield criteria and Ramberg-Osgood relation to describe plastic deformation. This is done through iterative adjustments of material parameters until agreement with experimental data is reached. Finally, a sensitivity study is conducted to evaluate the effects of different RVE sizes and resolutions on the accuracy and efficiency of the model.

The findings of this study suggest that the proposed workflow serves as a base for calibrating anisotropic material properties at the micro-scale to match macro-scale data. The derived material properties of fibers indicate a longitudinal elastic modulus on the order of 50 GPa and a transversal elastic modulus of approximately 4 GPa. For the plastic characteristics of fibers the calibrated properties closely approximate ideal plasticity.

The sensitivity analysis reveals that a volume of at least $0.33x0.33x0.12$ mm is required to be considered representative of the paperboard investigated in this study. However, due to material inhomogeneities, the model is influenced by the location of extraction. Moreover, the conducted studies show a clear dependence on tested voxel resolutions.

Contents

1 Introduction

With the goal of minimizing the environmental footprint of carton packages [14], advancement of the proportion of renewable materials, particularly wood fiber, are necessary. The mechanical performance of cellulose materials is influenced by various factors, including their inherent inhomogeneity and stochastic nature. Understanding the relationship between the microstructure and mechanical properties of these materials is crucial for optimizing their performance in practical applications.

1.1 Problem Formulation

The aim of this project is to characterize and quantify the micro-structure of paperboard. This involves identifying fibers and their orientations using X-ray Computerized Tomography scans, more commonly known as CT-images, as well as calibrating microscopic material properties. The smallest volume that accurately reflects the macroscopic behavior of the material, knows as the Representative Volume Element (RVE), should be investigated. The steps included are:

- Create a Finite Element model, including fiber orientations, based on X-ray tomography scans of paperboard

- Calibrate material properties of the fibers towards experimental macro-scale data

- Perform sensitivity studies on RVE sizes and image resolutions

Ultimately, the objective is to establish a systematic workflow for generating virtual models based on CT-scans, of paperboard.

1.2 Introduction to Paper Materials

In the paper making process, wood fibers are mixed and stirred with water to achieve fiber suspension. The mixed liquid is later sprayed on a wire or forming fabric. Excess water is removed by vacuum suction or drainage through the wire mesh and the paper material is pressed and dried. During this process, bonds are formed between the fibers [17].

The characteristics of the flow significantly influence the properties of paper as most of the fibers align in the direction of the flow, known as the manufacturing direction (MD). The ratio of fibers in the MD to those in the cross direction (CD) is referred to as fiber orientation anisotropy and affects the paper properties on macroscopic level. The orientation ratio is also influenced by factors such as the velocity and acceleration of the paper machine [36].
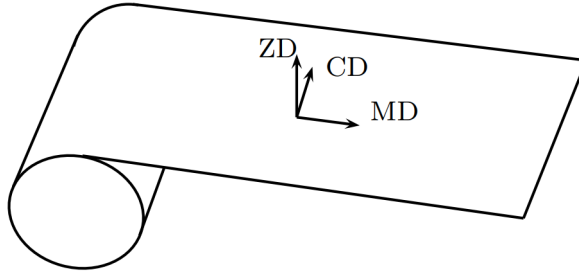
Figure 1: *Manufacturing directions of paper [7]*

Paperboard is a porous material that consists of a fiber network surrounded by air [33]. Under moderate mechanical loading its mechanical behavior can be described by anisotropic linear elasticity, and under high loading a non-linear plastic response. In previous work by Borgqvist [7], a 3D-continuum elasto-plastic model for paperboard was presented. The experimental data by Borgqvist will be used for calibration later in this study and is presented in Figure 2. The stress-strain response illustrates the typical behavior of paperboard and its anisotropy.
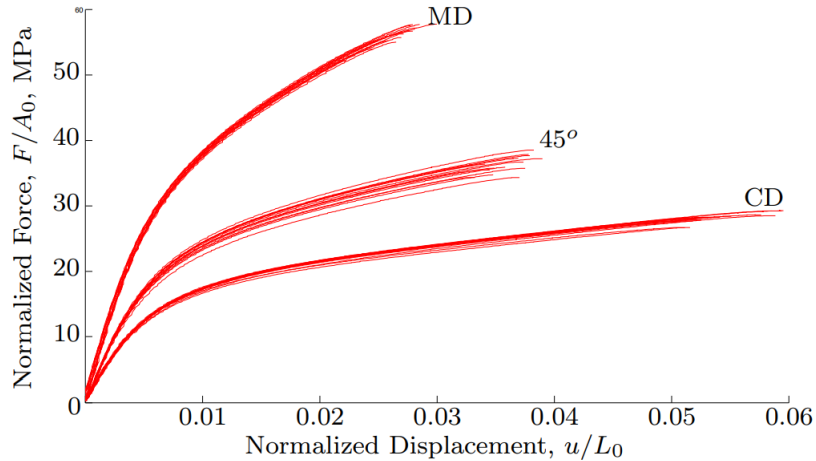
Figure 2: *In-Plane uniaxial tension tests of paperboard in MD, CD and 45° directions [7, Figure 4].*

In order to properly model the material behavior, knowledge about fiber orientation and fiber anisotropy are of importance. One aspect in modelling fiber materials is the characteristics related to the fiber-fiber bonds. To correctly capture and analyze these effects it is essential to segment and track individual fibers [33]. Fiber tracking is also of importance to examine the effects of moisture and temperature on individual fibers [17].

Softwood and hardwood fibers are commonly utilized in the pulp making process. Hardwood are stronger and more hard-wearing than softwoods. The mean

length and average fiber diameter of softwood typically ranges from 2 to 6 mm and $20\text{-}40\mu m$ respectively. In contrast, hardwood fibers possess mean lengths within the range of 1 to 2 mm and average fiber diameter ranging from 10-50 μm [9] Moreover, the physical properties of wood fibers such as density, Young's modulus and tensile strength are important characteristics that influence the mechanical behavior of paper products [9].

Direct testing of individual fibers is the most straightforward method for characterizing individual fiber properties. Due to the size of the fibers this method is rather complex and is rarely used. Macroscopic methods, such as compression or tensile testing of paperboard, combined with appropriate mechanical models, are commonly used.

Neagu et al. [19] used two different methods to determine the stiffness of wood fibers. They used one compression method combined with a statistical model based on first order beam-theory to describe the deformation. The second method was based on tensile testing and back calculation to predict fiber stiffness. For softwood kraft fibers, Young's modulus was 20.1 GPa with the compression method, and 17.4-19.0 GPa with the tensile method. In a different study Neagu et al. [25] used a similar approach to back calculate the fiber stiffness's from tensile testing of laminate composites. They concluded that industrially pulped hardwood fibers have higher stiffness than the corresponding softwood fibers. Young's modulus of 40 GPa was found for hardwood. Shaler [34] performed tension tests on individual fibers aiming to compare the strength and stiffness of earlywood and latewood fibers, which are a softwood fiber formed during different parts of the growing season. The earlywood fibers had an average modulus of elasticity of 14.8 GPa and an ultimate tensile stress of 604 MPa. The examined latewood fibers exhibited modulus of elasticity and ultimate tensile stress values that were 33% and 73% higher, respectively. Czibula et al. [8] addresses that existing literature primarily focuses on uniaxial tensile testing of single fibers, they often tend to neglect the effects of real process history on fiber properties when pulp fibers are used in paper materials. To address this, their study employs nanoindentation (NI) techniques on pulp fibers within paper sheets. Comparisons were made with longitudinal single fiber tensile testing data and inverted network models. Results from the NI provided an estimation of Young's modulus of 8-9 GPa, which was consistent with single fiber tensile testing result where the mean modulus was 8.3GPa. This result deviated slightly when compared to result from previous studies, which reported mean values ranging from 12 to 20 MPa. The network model showed higher estimation of 15.2 GPa.

The properties of the fibers in the shear and transverse direction are as previously stated not easily determined by experiments. The modulus of elasticity in transverse direction is commonly approximated to be about one-tenth as great as in the longitudinal direction [23]. The properties of fibers found in previous works are summarized in Table 1 and 2.

Table 1: *Young's modulus of fibers in longitudinal direction.*

E_F [GPa]	Source
Softwood	
17.4-20.1	Neagu et al. [19]
14.8-25.6	Shaler [34]
8-9	Czibula et al. [8]
Hardwood	
40	Neagu et al [19]

Table 2: *Young's modulus of fibers in transverse direction.*

E_T [GPa]	Source
$0.1E_F$	Persson [23]

1.3   Image Acquisition and Image Processing

This section explains how CT equipment can be used to obtain 3D representations of paperboard. It explains the process of X-ray computed tomography, and the subsequent segmentation to distinguish fiber and void within the scanned images.

1.3.1   X-ray Computerized Tomography

X-ray tomography is a non destructive method for extracting data about the structure of a sample on different scales. The principle of X-ray tomography is that a specimen is placed on a rotating stage, in the trajectory of an X-ray beam, between a source and a detector as seen in Figure 3. Some X-rays are absorbed by the specimen, and some are transmitted. The transmitted X-rays are captured by the detector, and converted to visible light using a scintillator. As the specimen rotates, several hundred or thousands of projections are recorded. [13].
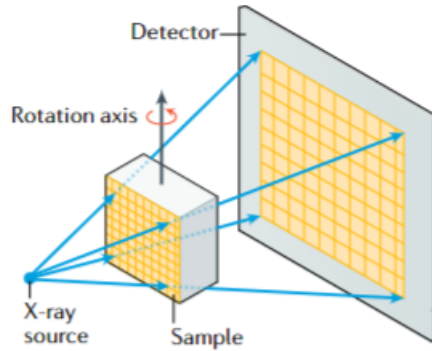
Figure 3: *Cone beam system, typically used in laboratory equipment [24]*

By utilizing mathematical algorithms and stacking the series of two dimensional images taken from different angles around the sample, a three dimensional reconstruction of reality is obtained including both the exterior and interior of the scanned object. The information about the structure is stored in cubic elements, called voxels [24]. Each voxel contains a value representing a grey shade. The shade depend on how much of the X-rays that have been transmitted, which in it's turn depend on the density of the structure. The features to be characterized have to be significantly larger than the size of the voxels to be properly distinguished. A smaller voxel size enables the analysis of finer details, but limits the area encompassed in the image. The scale of the captured features depends on the spatial resolution, which is the shortest linear distance between distinguishable points in a reconstructed image [24].

1.3.2 Segmentation

The method of separating structures and constituents from the reconstructed volume from each other, is called segmentation. Different approaches can be applied, including one of the most simple methods called thresholding. When applying thresholding segmentation, pixels in the 2D image are separated into groups based on their grey scale values [28]. Threshold values can be set manually or automatically, where one automatic approach is Otsu's method. Otsu's method picks the threshold value by maximizing the separation between different gray scales in the image and relies only on basic statistical information from the image's histogram of intensity distribution [21].

Even though automatic segmentation such as thresholding is widely used, a semi-automated interactive segmentation method may be beneficial for more complex tasks, for example separating individual fibers. However, to segment individual fibers in a composite is challenging as the bundles are in contact over large areas [29]. Li et al. performed a graph-based segmentation for individual fibers by sampling intensities along each fiber centre line and segmenting the surfaces using binary optimization [16]. Lately, deep learning approaches have shown promising results in segmenting complex structures from volumetric data such as CT-

scans. The deep-learning based segmentation methods require manual labeling of fibers and as training data could be difficult in low resolution images, it requires high resolution images [26]. Individual bundle segmentation can be performed by some commercial softwares, such as Avizo^{TM} from Thermo Fisher Scientific and VGStudio Max by Volume Graphics, but is computational expensive and require high resolution images [27]. The software package Avizo^{TM} reconstructs the fibers by applying a cylindrical template to CT-data, computing local cross-correlations to identify regions resembling fibers, and tracing their center lines for three-dimensional reconstruction [27]. Avizo^{TM} also has a package for AI-assisted segmentation [2].

2 Theory

Theory providing the foundation for the current work is presented. The establishment of a virtual finite element (FE) model from X-ray Computerized Tomography will be explained, involving image processing and the mapping of voxels to finite elements. Additionally, the derivation of fiber orientation computations and anisotropic material models will be provided.

2.1 RVE - Representative Volume Element

A Representative Volume Element (RVE) is the smallest volume of a material with invariant constitutive properties. The requirement for an RVE is that it should exhibit statistically representative material properties, maintaining consistent behavior as its size increases. Additionally, for a homogeneous material, the material properties within the RVE should be statistically independent of the location from where the sample is extracted. Thus, the average behavior of the RVE should be representative of the entire material [17].

Because there are more bindings in MD than CD and ZD the critical size in MD is expected to be the largest [17]. However, to overcome computational challenges the RVE is often approximated as a unit- cell with certain repeating patters, even though capturing the micro-structure features less accurately. The main reasons are simplicity and computational efficiency [5].

Common metrics for determining the size of RVEs in composites include the number of fibers or the ratio of RVE characteristic length to fiber radius (δ). Studies on RVE size have explored various factors such as microstructural features, constituent materials, finite element model setup, and damage/failure criteria. These studies have reported diverse RVE sizes, ranging from 9 to 60 for δ - values and from 30 to 200 number of fibers, typically within a 60% fiber volume fraction [5]. Balasubramani et al. [5] studied the size and shape effects of random 3D statistical volume elements by performing simulations on fiber reinforced polymers at approximately 60% fiber-volume fraction. Their analysis focused on the statistical convergence of geometric features and the predicted structural properties in comparison with commonly used unit-cell models. Their findings suggest that models with more than 11 fibers must be considered to properly capture the properties of interest. Koohbor et al. [6] investigate the size of RVE length scale in fiber composites using SEM and digital image correlation. By analyzing average strain fields they found that the RVE size were equivalent to an area encompassing 15 to 30 randomly distributed fibers. Additionally, the study revealed that the RVE size increases with higher global stress. Prior studies have adopted multiscale methodologies to analyze fiber properties. For example, Sevenois et al. [32] employed a multiscale approach to determine the 3D transverse isotropic elastic properties of carbon fibers. Their investigation involved a RVE containing 30 fibers. The RVE sizes found in previous works are summarized in Table 3.

Table 3: *RVE sizes used in previous studies.*

RVE size	Source
Number of fibers	
>11	Balasubramani et al. [5]
15-30	Koohbor et al. [6]
30	Sevenois et al. [32]
Ratio length to fiber radius, δ	
9-60	Balasubramani et al. [5]

2.2 Meshing and Finite Element Modelling

To transform the data from the CT-images to a finite element model, a mesh of the geometry have to be created. Fiber orientations are then calculated and mapped to the elements. There are two common approaches for creating a finite element mesh, voxel to mesh mapping, and geometry segmentation based meshing [31]. A voxel based mesh can easily be generated from CT-data and does not require as much manual work and preparation as the geometry based mesh. The method is based on creating a finite element from each voxel [3]. The disadvantage of the approach is that it can lead to large model sizes, and that there is not an accurate representation of the boundary between the constituents of the micro structure [30]. The geometry based segmentation method is based on meshing the geometry of the structures related to segmented surfaces.

Doitrand et al. [10] studied the accuracy of voxel- and geometry based meshing. The study showed that the voxel mesh resulted in a less precise approximation of the geometry and leading to differences in damage prediction compared to the geometry based mesh. The authors stated that voxel based mesh is suited for calculations of the average elastic behavior of the composite, but not if local stress concentrations are of interest. Ewert et al. [3] did a similar comparison between the two meshing techniques and came to a similar conclusion. The authors concluded that voxel based meshing can be a good substitute to geometry based meshing when estimating the overall thermo-elastic properties of 3D woven composites. It was also stated that high resolution voxel models have a great number of degrees of freedom, resulting in a long computational time. Nevertheless, since mesh preparation is quicker, the overall time required may still be less than that for geometry-based meshing.

2.3 Orientation Analysis

There are different methods for determining the material directions, and they can be categorized into direct- and indirect methods. The direct method is based on tracking individual fibers, and therefore require high resolution images. One commonly used indirect method for fiber tracking is structure tensor analysis.

Karamov et al. [27] compared the results of two high-fidelity, direct methods with the structure tensor approach for a short fiber composite. The high-fidelity methods used were ellipsometry and 3D fiber assembly reconstruction. Ellipsometry, is a method based on measuring the ellipsoidal cross section of individual fibers by analyzing changes in polarization state. The method may result in a large amount of data and normally requires some manual work. Ellipsometry-based methods are limited by challenges in accurately determining fiber orientation from elliptical cross-sections and reduced precision for fibers near normal or parallel to the cross-section plane. The second method, 3D fiber assembly reconstruction, is based on individual bundle segmentation. The center line traced in the segmentation process, can be imported as the direction of the fiber. This method is for example used by the Avizo software. The structure tensor approach yielded similar results as the high-fidelity methods for images with resolution allowing individual fiber recognition. For lower resolution images, with pixel size close to the fiber diameter, only the structure tensor method could generate orientations, which where consistent with the results from the high-fidelity methods on high resolution images [27].

The structure tensor approach for orientation analysis will be explained in section 2.3.4. The basis on the structure tensor involves analyzing image gradients, which often employs filtering to reduce noise and to enhance image quality. In section 2.3.1 and 2.3.2 two different methods to filter the image and establish the gradients of intensities will be explained.

2.3.1 Gradients with Gaussian Kernel

In this section, a voxel-based approach is utilized to compute the image gradients. A commonly used method in this domain is the Gaussian derivative kernel approach, which computes filtered voxel gradients using derivatives of the Gaussian kernel. This kernel includes a parameter denoted as $\sigma > 0$, representing the noise scale, which determines the deviation of the Gaussian Kernel as seen in Figure 4 [20].
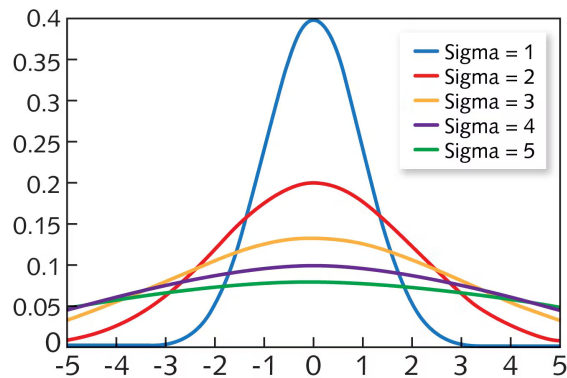

Figure 4: *Filtering effect of sigma on Gaussian Kernel [4].*

The value of the noise scale should be large enough to suppress high frequency

noise, but small enough to compute gradients locally [30]. Jeppesen et al. chose a noise scale related to the average fiber radius r_f [20]

$$\sigma = \frac{r_f}{\sqrt{2}} \tag{2.3.1}$$

A stack of gray scale images, representing a three dimensional geometry is mapped to a matrix. The matrix contain values representing the intensity in each voxel, $I(\boldsymbol{x_0})$. The Gaussian kernel method is then used to smooth the intensity by calculating the convolution within a neighbourhood of each image point, $\boldsymbol{x_0}$. For a three dimensional space it results in the following integral

$$\tilde{I}(\boldsymbol{x_0}) = \frac{1}{V_\sigma} \int_V K_\sigma(|\boldsymbol{x_0} - \boldsymbol{x}|) I(\boldsymbol{x}) dV \tag{2.3.2}$$

with K_σ representing the Gaussian Kernel function.

The equation expresses filtering of the intensities over a volume, where $\tilde{I}(\boldsymbol{x})$ is the filtered intensity. $\boldsymbol{x_0}$ is the voxel for which the function is to be evaluated and $\boldsymbol{x}$ the voxels in a surrounding region $\mathbb{R}^3$ [12]. [11]. In this context, V_σ denotes the volume of all surrounding voxels included in the filtering for a specific voxel. Due to the focus on intensity gradients, considerations pertaining to normalized intensities are unnecessary. Consequently, the subsequent derivation will not incorporate the constant $\frac{1}{V_\sigma}$. The volume integral is approximated by a sum of the weighted intensities

$$\tilde{I}(\boldsymbol{x_0}) = \int_V K_\sigma(|\boldsymbol{x_0} - \boldsymbol{x}|) I(\boldsymbol{x}) dV \approx \sum_i^k K_\sigma(|\boldsymbol{x_0} - \boldsymbol{x_i}|) I(\boldsymbol{x_i}) \tag{2.3.3}$$

where the parameter k represents all elements $\boldsymbol{x_i}$ to be accounted for [20]. The Gaussian Kernel, $K_\sigma(|\boldsymbol{x_0} - \boldsymbol{x}|)$ function is given by [12]

$$K_\sigma(|\boldsymbol{x_0} - \boldsymbol{x}|) = \frac{1}{2\pi\sigma^2} e^{-\frac{|\boldsymbol{x_0} - \boldsymbol{x}|^2}{2\sigma^2}} \tag{2.3.4}$$

Given a constant intensity I per voxel, the gradient of the smoothed function is given below, and the format of the gradient is obtained as [20]

$$\nabla \tilde{I} = [\tilde{I}_x \quad \tilde{I}_y \quad \tilde{I}_z]^T = \sum_i^k \nabla K_\sigma \cdot I(\boldsymbol{x_0} - \boldsymbol{x_i}) \tag{2.3.5}$$

To ensure that the gradient vectors accurately point in the intended direction, the surrounding volume of point $\boldsymbol{x_0}$ must be spherical. Otherwise, asymmetry in the contribution to the kernel derivative may occur, causing the gradient vector to extend outward from the volume rather than in the direction of maximum intensity change. To prevent nonphysical boundaries in the model, the gradients are computed over a larger volume. After the gradient calculations, this volume is cropped to the region of interest, and the structure tensor is calculated specifically within this region of interest

2.3.2 Gradients with Abaqus Transient Heat Equation

A different approach to calculating gradients of intensity involves utilizing built in functions in Abaqus. The basics of this method is to use the transient heat equation to examine heat flux. By setting the temperature analogous to pixel intensity and applying a time dependent heat equation to the image, the pixel values will be smooth. The result is similar to when applying Gaussian filter to the image.

Preceding from the energy equation with body forces and gravitational forces neglected, and constant density assumed [35],

$$\rho \frac{DE}{Dt} = -\frac{\partial}{\partial x_i}(pv_i) + \frac{\partial}{\partial x_j}(\tau_{ij}v_i) + \frac{\partial}{\partial x_i}(k\frac{\partial T}{\partial x_i}) + S_E \qquad (2.3.6)$$

Neglecting viscous stresses ($\tau_{ij} = 0$), assuming no heat source ($S_E = 0$) and no net rate of flow ($\frac{\partial}{\partial x_i}(pv_i) = 0$), the energy equation is reduced to

$$\rho \frac{DE}{Dt} = \frac{\partial}{\partial x_i}(k\frac{\partial T}{\partial x_i}) \qquad (2.3.7)$$

Here, the specific energy E is defined as the sum of internal energy E_i and kinetic energy, represented by $E_k = \frac{1}{2}(u^2 + v^2 + w^2)$. With no velocity components the system specific energy is equal to its internal energy E_i

$$E_i = cT \qquad (2.3.8)$$

where c is the specific heat and T the temperature. Inserting into equation (2.3.7) results in

$$\rho c \frac{dT}{dt} = div(k\nabla T) = div(-q) \qquad (2.3.9)$$

where Fourier's law $q = -k\nabla T$ [35] has been used.

By declaring the element type in Abaqus as purely diffusive 8 node linear brick elements (DC3D8) [1], Abaqus will solve the transient heat equation. When setting the specific heat c and density ρ to 1 , and solving the heat equation with implicit, Euler backward time discretisation scheme it results in

$$\frac{T - T_n}{\Delta t} = div(k\nabla T) \qquad (2.3.10)$$

The equation can be solved for one step, $\Delta t = 1$, resulting in the short expression

$$T = T_n + k\nabla^2 T \qquad (2.3.11)$$

Here, T_n represents the initial intensities and T the intensities solved for t=1. The thermal diffusivity depends on the thermal conductivity coefficient k. A higher k results in faster diffusion, and when k approaches zero T is approaching T_n which indicates a minimal diffusion and less smoothing. The heat flux vector $q = -k\nabla T$ representing the smoothed image gradients can be displayed and retrieved with Abaqus. In conclusion, in terms of intensity equation (2.3.11) takes the format

$$\tilde{I} = I + k\nabla^2 I \tag{2.3.12}$$

In order to address the heat equation, it is essential to set boundary conditions, typically involving either insulated surfaces or a temperature distribution. However, these choices may not accurately represent the intensity gradients at the boundaries. Similar to the challenge encountered when computing Gaussian Kernel Gradients, this issue can be resolved by determining gradients over a larger volume compared to the one used for establishing orientations.

2.3.3 Comparison of Gradient Methods

To be able to compare the gradient method, equations (2.3.3) and (2.3.12), it is of interest to find the relation between the conductivity coefficient, k and the noise scale, σ, controlling the filtering.

The intensity at a point $\boldsymbol{x}$ about a point $\boldsymbol{x_0}$ in space can be approximated by its second order Taylor expansion

$$I(\boldsymbol{x}) \approx I(\boldsymbol{x_0}) + \nabla I(\boldsymbol{x_0})(\boldsymbol{x} - \boldsymbol{x_0}) + \frac{1}{2!}\nabla^2 I(\boldsymbol{x_0})(\boldsymbol{x} - \boldsymbol{x_0})^2 + H.O.T \tag{2.3.13}$$

Combining equations (2.3.2) and (2.3.13) an expression for the averaged intensities is obtained as

$$\tilde{I}(\boldsymbol{x_0}) = \int_V K_\sigma I(\boldsymbol{x_0})dV + \int_V K_\sigma \nabla I(\boldsymbol{x_0})(\boldsymbol{x} - \boldsymbol{x_0})dV + \frac{1}{2!}\int_V K_\sigma \nabla^2 I(\boldsymbol{x_0})(\boldsymbol{x} - \boldsymbol{x_0})^2 dV \tag{2.3.14}$$

Due to isotropy of K_σ the integrals of odd terms vanish [11],

$$\tilde{I}(\boldsymbol{x_0}) = \int_V K_\sigma I(\boldsymbol{x_0})dV + \frac{1}{2!}\int_V K_\sigma \nabla^2 I(\boldsymbol{x_0})(\boldsymbol{x} - \boldsymbol{x_0})^2 dV \tag{2.3.15}$$

This expression using index notation with the point to be evaluated, $\boldsymbol{x_0}$, and the points in its surrounding, $\boldsymbol{x}$ is given as

$$\tilde{I}(\boldsymbol{x_0}) = \int_V K_\sigma I(\boldsymbol{x_0})dV + \frac{1}{2!}\int_V K_\sigma \frac{\partial^2 I}{\partial x_i \partial x_j}\bigg|_{\boldsymbol{x_0}} (x_i - x_i^0)(x_i - x_i^0)dV \tag{2.3.16}$$

With the pixel intensity at the current point, $I(\boldsymbol{x_0})$, being constant it can be moved outside the integral.

The first term in (2.3.16) describing the integral of the weight function K_σ over a infinite volume is expressed with the constant V_r

$$\int_V K_\sigma dV \cdot I(\boldsymbol{x_0}) = V_r \cdot I(\boldsymbol{x_0}) \tag{2.3.17}$$

computed as

$$V_r = \frac{\sigma \pi^{3/2}\sqrt{2}}{\pi} \tag{2.3.18}$$

12

Considering the second term (2.3.16), the integrals will vanish when $i \neq j$ due to the isotropy of K_σ,

$$\frac{1}{2!}\int_V K_\sigma \frac{\partial I}{\partial x_i \partial x_j}\bigg|_{\boldsymbol{x_0}}(x_i - x_i^0)(x_i - x_i^0)dV = \frac{1}{2!}\left(\int_V K_\sigma(x_1 - x_1^0)^2 dV \cdot \frac{\partial^2 I}{\partial x_1^2}\bigg|_{\boldsymbol{x_0}}\right.$$

$$+ \int_V K_\sigma(x_2 - x_2^0)^2 dV \cdot \frac{\partial^2 I}{\partial x_2^2}\bigg|_{\boldsymbol{x_0}}$$

$$\left. + \int_V K_\sigma(x_3 - x_3^0)^2 dV \cdot \frac{\partial^2 I}{\partial x_3^2}\bigg|_{\boldsymbol{x_0}}\right)$$

(2.3.19)

The three integrals in equation (2.3.19) can be expressed as a constant Q,

$$Q = \frac{1}{2!}(\int_{-\infty}^{\infty}\int_{-\infty}^{\infty}\int_{-\infty}^{\infty} K_\sigma(x_1 - x_1^0)^2 dx_1 dx_2 dx_3) =$$

$$\frac{1}{2!}(\int_{-\infty}^{\infty}\int_{-\infty}^{\infty}\int_{-\infty}^{\infty} K_\sigma(x_2 - x_2^0)^2 dx_1 dx_2 dx_3) = \qquad (2.3.20)$$

$$\frac{1}{2!}(\int_{-\infty}^{\infty}\int_{-\infty}^{\infty}\int_{-\infty}^{\infty} K_\sigma(x_3 - x_3^0)^2 dx_1 dx_2 dx_3)$$

with

$$Q = \frac{\sigma^3 \pi^{3/2}\sqrt{2}}{2\pi} \qquad (2.3.21)$$

The simplified format of the filtered intensities (2.3.14) evaluated at $\boldsymbol{x_0}$ is now

$$\tilde{I} = V_r I + Q\left(\frac{\partial^2 I}{\partial x_1^2} + \frac{\partial^2 I}{\partial x_2^2} + \frac{\partial^2 I}{\partial x_3^2}\right) = V_r I + Q(\text{div}(\text{grad}(I))) \qquad (2.3.22)$$

which is equivalent to

$$\frac{1}{V_r}\tilde{I} = I + \frac{Q}{V_r}\text{div}(\text{grad}(I)) \qquad (2.3.23)$$

As $\frac{1}{V_r}$, by which the filtered intensity is multiplied, remains constant, it uniformly scales all filtered intensities and can be disregarded. Equation (2.3.23) can now be written on the same format as the heat equation

$$\tilde{I}_0 = I + k\nabla^2 I \qquad (2.3.24)$$

where the constant k in (2.3.24) is equal to the conductivity in the heat equation. The conductivity can from the expressions for V_r (2.3.18) and Q (2.3.21) be expressed as

$$k = \frac{Q}{V_r} = \frac{1}{2}\sigma^2 \qquad (2.3.25)$$

To yield the same amount of filtering, conductivity k and noise scale σ, should be related according to this relation.

2.3.4 Structure Tensor

Once the image gradients have been established the Structure Tensor approach can be used to find the fiber orientation. A structure tensor is a 3- by- 3 matrix that captures the local orientation around a point in space. In the voxel based approach the structure tensor is computed for each voxel in the image. The summation is performed in a certain neighbourhood around the point. [18]. Once again using the Gaussian Kernel, but this time with ρ, known as the integration scale, controlling the standard deviation of the filter[20],

$$\boldsymbol{S} = \sum_{i=1}^{k} K_\rho * (\nabla \tilde{I}(\nabla \tilde{I})^T) \qquad (2.3.26)$$

with

$$K_\rho(|\boldsymbol{x_0} - \boldsymbol{x}|) = \frac{1}{2\pi\rho^2} e^{-\frac{|\boldsymbol{x_0}-\boldsymbol{x}|^2}{2\rho^2}} \qquad (2.3.27)$$

The size of ρ is chosen as small enough to reduce the influence of the surrounding fibers, but large enough to capture the structural direction. Jeppesen et al. [20] suggested a size related to the noise scale:

$$\rho = 4\sigma \qquad (2.3.28)$$

Given a unit vector $\mathbf{u}$, the product $\mathbf{u}^T \mathbf{S} \mathbf{u}$ measures the squared intensity change for a small displacement in the direction $\mathbf{u}$. By determining the eigenvalues to $\mathbf{S}$ both the direction corresponding to the smallest and largest intensity variation can be identified. The eigenvector corresponding to the smallest eigenvalue coincide with the the least change in intensity, which indicates the fiber longitudinal direction. In turn, the eigenvector of the largest eigenvalue corresponds to the largest change in intensity, perpendicular to the fiber axial direction [18]. The eigenvectors and eigenvalues for a two dimensional elliptical example is presented in Figure 5.
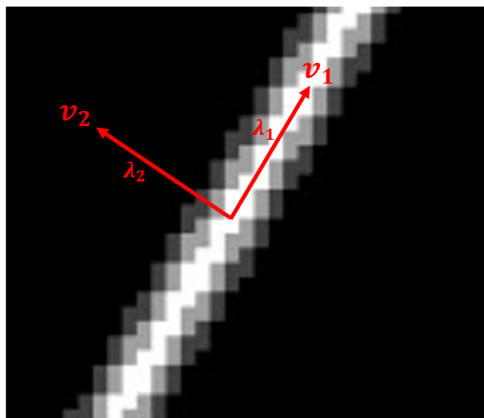

Figure 5: *Eigenvectors with corresponding eigenvalues for an elliptical model in two dimensions. $\boldsymbol{v_1}$ represents the eigenvector corresponding to the smallest eigenvalue λ_1. $\boldsymbol{v_2}$ represents the eigenvector corresponding to the largest eigenvalue λ_2*

2.4 Material Models

In the following derivation of the material model for fibers transversal isotropic behavior is considered, meaning the material will behave differently along and perpendicular to the fiber axis. The total strain in the material can be divided into elastic and plastic strains

$$\boldsymbol{\epsilon} = \boldsymbol{\epsilon}^e + \boldsymbol{\epsilon}^p \tag{2.4.1}$$

written in voigt notation, and the stress in the material can from Hooke's law can be expressed as

$$\boldsymbol{\sigma} = \boldsymbol{D}\boldsymbol{\epsilon}^e = \boldsymbol{D}(\boldsymbol{\epsilon} - \boldsymbol{\epsilon}^p) \tag{2.4.2}$$

Before the yield stress, σ_{y0}, is reached, the material will only have an elastic contribution to the total strain and behave in a linear manner. For stresses above the yield stress, the material behaves non-linearly as plastic deformations are present. The two regions are referred to as the elastic and plastic regions, and their material models are derived in this section.

While the material parameters are set locally in the fiber direction, the global response of the RVE can be approximated by the engineering stress and strain

$$\sigma = \frac{F}{A_0} \tag{2.4.3}$$

$$\epsilon = \frac{\Delta L}{L_0} \tag{2.4.4}$$

2.4.1 Elastic Material Model

In the elastic region, the behavior is defined using the Abaqus 'engineering constants' for orthotropic materials. This requires setting the elastic moduli (E_{11}, E_{22}, E_{33}) in respective directions, along with the corresponding Poisson's ratios $(\nu_{12}, \nu_{13}, \nu_{23})$ and shear moduli (G_{12}, G_{13}, G_{23}).

The independent stiffness parameters in the constitutive matrix for a transverse isotropic material can be derived from the coordinate transformation $\boldsymbol{x'} = \boldsymbol{Ax}$ with symmetry about the 1-axis. The transformation matrix A is given by,

$$\boldsymbol{A} = \begin{bmatrix} 1 & 0 & 0 \\ 0 & cos(\alpha) & sin(\alpha) \\ 0 & -sin(\alpha) & cos(\alpha) \end{bmatrix} \tag{2.4.5}$$

Using the relationships $\boldsymbol{\sigma'} = \boldsymbol{A}\boldsymbol{\sigma}\boldsymbol{A^T}$ and $\boldsymbol{\epsilon'} = \boldsymbol{A}\boldsymbol{\epsilon}\boldsymbol{A^T}$ alongside Hooke's law in equation (2.4.2), and computing the stresses and strains resulting from rotations about the 1-axis, combined with major symmetry properties, reveals that transversely isotropic materials exhibit six independent stiffness components,

$$\boldsymbol{D} = \begin{bmatrix} D_{11} & D_{12} & D_{12} & 0 & 0 & 0 \\ D_{12} & D_{22} & D_{23} & 0 & 0 & 0 \\ D_{12} & D_{23} & D_{22} & 0 & 0 & 0 \\ 0 & 0 & 0 & D_{44} & 0 & 0 \\ 0 & 0 & 0 & 0 & D_{44} & 0 \\ 0 & 0 & 0 & 0 & 0 & D_{66} \end{bmatrix} \tag{2.4.6}$$

The 2-3 plane is defined as the plane of isotropy, denoting the direction perpendicular to the fibers, i.e the transverse direction T. Additionally, the longitudinal direction L is specified as the 1- direction, and the unknown parameters can then be reduced to $E_{11} = E_L$, $E_{22} = E_{33} = E_T$, $\nu_{12} = \nu_{13} = \nu_{LT}$, $\nu_{23} = \nu_{TT}$, $G_{12} = G_{13} = G_{LT}$ and $G_{23} = G_{TT}$.

The constitutive matrix $\boldsymbol{D}$ for a transverse isotropic material can now be expressed as

$$\boldsymbol{D} = \begin{bmatrix} \frac{E_L E_T (\nu_{TT}-1)}{\Delta} & -\frac{E_L E_T \nu_{LT}}{\Delta} & -\frac{E_L E_T \nu_{LT}}{\Delta} & 0 & 0 & 0 \\ -\frac{E_L E_T \nu_{LT}}{\Delta} & -\frac{E_T(E_T - E_L \nu_{LT}^2)}{(\nu_{TT}+1)\Delta} & -\frac{E_T(E_T \nu_{TT}+1 + E_L \nu_{LT}^2)}{(\nu_{TT}+1)\Delta} & 0 & 0 & 0 \\ -\frac{E_L E_T \nu_{LT}}{\Delta} & -\frac{E_T(E_T \nu_{TT}+1 + E_L \nu_{LT}^2)}{(\nu_{TT}+1)\Delta} & -\frac{E_T(E_T - E_L \nu_{LT}^2)}{(\nu_{TT}+1)\Delta} & 0 & 0 & 0 \\ 0 & 0 & 0 & G_{LT} & 0 & 0 \\ 0 & 0 & 0 & 0 & G_{LT} & 0 \\ 0 & 0 & 0 & 0 & 0 & G_{TT} \end{bmatrix} \tag{2.4.7}$$

where Δ is given as

$$\Delta = 2E_L \nu_{LT}^2 - E_T + E_T \nu_{TT} \tag{2.4.8}$$

As one of the aims of this project is to calibrate material parameters it is of interest to simplify the constitutive relation by reducing the number of independent parameters. Therefore the approximation is made that $\nu_{LT} = \nu_{TT} = 0.3$. For simplification G_{TT} is set equal to G_{LT} given by Lekhnitskii approximation [15],

$$G_{LT} = \frac{1}{4\frac{1}{E_{45}} - \frac{1}{E_L}(1 - \nu_{LT}) - \frac{1}{E_T}(1 - \nu_{LT})} \tag{2.4.9}$$

where E_{45} is the elastic modulus in the 45-degree direction of a fiber and is approximated by [36],

$$E_{45} = \frac{1}{\frac{1}{2}\left(\frac{1}{E_L E_T}\right)^{1/2} + \frac{1}{4}\left(\frac{1}{E_L} + \frac{1}{E_T}\right)} \tag{2.4.10}$$

This leaves two independent elastic parameters to be calibrated, E_L and E_T.

2.4.2 Plastic Material Model

Initial yielding is assumed to be characterized by the symmetric fourth-order tensor which in matrix format can be represented by $\boldsymbol{P}$ in the following yield criterion [22],

$$\boldsymbol{\sigma}^T \boldsymbol{P} \boldsymbol{\sigma} - 1 = 0 \tag{2.4.11}$$

Due to symmetry properties, the 6x6 matrix $\boldsymbol{P}$ consists of 21 independent parameters in its general, anisotropic case. The stress can be split into its two parts, its deviatoric component $\boldsymbol{s}$ and hydrostatic component $\boldsymbol{e}$

$$\boldsymbol{\sigma} = \boldsymbol{s} + \boldsymbol{e}, \quad \boldsymbol{s} = \begin{bmatrix} s_{11} \\ s_{22} \\ s_{33} \\ s_{12} \\ s_{13} \\ s_{23} \end{bmatrix}, \quad \boldsymbol{e} = \frac{1}{3} I_1 \begin{bmatrix} 1 \\ 1 \\ 1 \\ 0 \\ 0 \\ 0 \end{bmatrix}, \tag{2.4.12}$$

where I_1 is the first invariant of the stress tensor.

By assuming that the material behaves orthotropically and that only deviatoric stresses influence initial yielding [1] ($\boldsymbol{P}\boldsymbol{e} = 0$), the initial yield criterion (2.4.11) can be written as [1]

$$\boldsymbol{s}^T \boldsymbol{P} \boldsymbol{s} - 1 = 0 \tag{2.4.13}$$

and $\boldsymbol{P}$ is reduced to include only 6 independent material parameters and is given by [22] [1],

$$\boldsymbol{P} = \begin{bmatrix} F+G & -F & -G & 0 & 0 & 0 \\ -F & F+H & -H & 0 & 0 & 0 \\ -G & -H & G+H & 0 & 0 & 0 \\ 0 & 0 & 0 & 2L & 0 & 0 \\ 0 & 0 & 0 & 0 & 2M & 0 \\ 0 & 0 & 0 & 0 & 0 & 2N \end{bmatrix} \tag{2.4.14}$$

By inserting (2.4.14) into (2.4.13) the Hill orthotropic yield criterion is given by [22],

$$f(s_{ij}, K_\alpha) = F(s_{11}-s_{22})^2 + G(s_{11}-s_{33})^2 + H(s_{22}-s_{33})^2 + 2Ls_{12}^2 + 2Ms_{13}^2 + 2Ns_{23}^2 - 1 = 0 \tag{2.4.15}$$

which is equal to zero at the onset of plastic strains.

From equation (2.4.15) it can be determined that F, G, H, L, M, N is dependent on the initial yield stress in each direction aligned with the material axes, and can be expressed as [22]

$$F = \frac{1}{2}\left(\frac{1}{\sigma_{y0}^{11^2}} + \frac{1}{\sigma_{y0}^{22^2}} - \frac{1}{\sigma_{y0}^{33^2}}\right)$$

$$G = \frac{1}{2}\left(\frac{1}{\sigma_{y0}^{11^2}} + \frac{1}{\sigma_{y0}^{33^2}} - \frac{1}{\sigma_{y0}^{22^2}}\right)$$

$$H = \frac{1}{2}\left(\frac{1}{\sigma_{y0}^{22^2}} + \frac{1}{\sigma_{y0}^{33^2}} - \frac{1}{\sigma_{y0}^{11^2}}\right) \tag{2.4.17}$$

$$L = \frac{1}{2\tau_{y0}^{12^2}}$$

$$M = \frac{1}{2\tau_{y0}^{13^2}}$$

$$N = \frac{1}{2\tau_{y0}^{23^2}}$$

As the material is assumed transverse isotropic, it holds that $\sigma_{y0}^{22} = \sigma_{y0}^{33} = \sigma_{y0}^{T}$ and consequently F=G. The same holds for $\sigma_{12} = \sigma_{13} = \sigma_{LT}$ resulting in $L = M$. The consitiutive matrix is now reduced to four unknowns, F, H, L and N

$$\boldsymbol{P} = \begin{bmatrix} 2F & -F & -F & 0 & 0 & 0 \\ -F & F+H & -H & 0 & 0 & 0 \\ -F & -H & F+H & 0 & 0 & 0 \\ 0 & 0 & 0 & 2L & 0 & 0 \\ 0 & 0 & 0 & 0 & 2L & 0 \\ 0 & 0 & 0 & 0 & 0 & 2N \end{bmatrix} \tag{2.4.18}$$

Material hardening characteristics can be represented by rewriting the initial yield criterion (2.4.13) [22],

$$f(\sigma_{ij}, K) = (\sigma_{y0}^2 \boldsymbol{s}^T \boldsymbol{P} \boldsymbol{s})^{1/2} - \sigma_y = 0 \tag{2.4.19}$$

where σ_y represent the current yield stress. Assuming isotropic hardening, meaning that the yield stress increases uniformly in all directions as plastic deformation occurs, the yield stress can be represented by

$$\sigma_y = \sigma_{y0} + K(\kappa) \tag{2.4.20}$$

σ_{y0} is the user defined reference initial yield stress, K_α denotes the hardening parameters and κ represent the internal variables describing the state of the material dependent on the plastic loading history.

In Abaqus the Hill Anisotropic yield criterion is defined by the yield stress ratios ($\frac{\bar{\sigma}_{ij}}{\sigma_{y0}}$) called potential parameters, where $\tau_{y0} = \frac{\sigma_{y0}}{\sqrt{3}}$ [1]. The definitions of the potential parameters are [1],

$$R_{11} = \frac{\sigma_{y0}^{11}}{\sigma_{y0}}$$

$$R_{22} = \frac{\sigma_{y0}^{22}}{\sigma_{y0}}$$

$$R_{33} = \frac{\sigma_{y0}^{33}}{\sigma_{y0}}$$

$$R_{12} = \frac{\sigma_{y0}^{12}}{\tau_{y0}}$$

$$R_{13} = \frac{\sigma_{y0}^{13}}{\tau_{y0}}$$

$$R_{23} = \frac{\sigma_{y0}^{23}}{\tau_{y0}}$$

(2.4.22)

With these definitions the yield criteria (2.4.19) can be expressed in potential parameters. In this project the longitudinal direction of the fiber will be chosen as the reference direction, resulting in that $R_{11} = R_L$ will be set to 1. It also follows that the the reference yield stress correspond to $\sigma_{y0} = \sigma_{y0}^{11} = \sigma_{y0}^L$. Reduction of the potential parameters with respect to transverse isotropy is expressed as

$$R_{11} = R_L = 1$$
$$R_{22} = R_{33} = R_T$$
$$R_{12} = R_{13} = R_{LT}$$
$$R_{23} = R_{TT}$$

(2.4.24)

The evolution equation for plastic strain is given by

$$\dot{\epsilon}_{ij}^p = \dot{\lambda}\frac{\partial f}{\partial \sigma_{ij}}$$

(2.4.25)

For an orthotropic material undergoing isotropic hardening it can be shown that the plastic multiplier

$$\dot{\lambda} = \dot{\epsilon}_{eff}^p$$

(2.4.26)

with the effective plastic strain rate (denoted equivalent plastic strain rate in Abaqus) defined as

$$\dot{\epsilon}_{eff}^p = \sqrt{\frac{2}{3}\dot{\epsilon}_{ij}^p\dot{\epsilon}_{ij}^p}$$

(2.4.27)

The remaining parameters to be determined is then the relation between the yield stress and plastic strain. The material behavior in the plastic region for in-plane tensile test directions MD, CD and 45° respectively are modelled using the Ramberg-Osgood relation.

$$\epsilon = \frac{\sigma}{E} + (\frac{\sigma}{E^0})^N$$

(2.4.28)

19

The aim is to utilize the same relationship for setting transverse isotropic material parameters at the fiber level while striving to minimize the error between the simulated global stress-strain curve and the data from tensile tests in MD and CD directions. A power type hardening function also known as the Ramberg-Osgood relation will therefore be used to capture the fiber hardening characteristics, describing the relation between the yield stress and plastic strains

$$\epsilon^p = (\frac{\sigma_y}{E_0})^N \tag{2.4.29}$$

The relation between yield stress at a given equivalent plastic strain ϵ^p_{eff} is inputted as tabular data in Abaqus

$$\sigma_y = \sigma_{y0} + K(\epsilon^P_{eff}) \tag{2.4.30}$$

with

$$K(\epsilon^P_{eff}) = (E_0 \epsilon^p_{eff})^{1/N} \tag{2.4.31}$$

with the reference yield stress $\sigma_y = \sigma_{y0}$ as initial value when $\epsilon^p_{eff} = 0$. When the yield stress is equal to the reference yield stress $\sigma_y = \sigma_{y0}$, it marks the the onset of plastic deformation, indicated by $\epsilon^p_{eff} > 0$.

To model the fibers as transversely isotropic there are now 6 independent parameters to be defined. The potential parameters

- R_T

- R_{LT}

- R_{TT}

to define the material anisotropy and

- σ^L_{y0}

- E_0

- N

to define the initial yielding and the hardening function. To reduce the number of unknowns further R_{TT} is approximated as

$$R_{TT} = \frac{\bar{\sigma}_{TT}}{\tau_0} = \frac{\sqrt{3}}{2}\frac{\bar{\sigma}_T}{\sigma_0} \tag{2.4.32}$$

where it is assumed that $\bar{\sigma}_{TT} = \frac{1}{2}\bar{\sigma}_T$.

2.5 Abaqus Solver

There are primarily two solvers available in Abaqus for solving system equilibrium: the implicit and explicit solver. Generally the implicit solver is most suitable for static or quasi-static simulations, where the response of the system evolves gradually over time and events with long duration's. In such cases the implicit solver is unconditionally stable meaning that it is independent on the time step chosen. In dynamic simulations, with rapidly changing system or large deformations the implicit solver may require smaller time steps to accurately capture the dynamic behavior of the system. In such cases the explicit solver is more stable and computationally efficient.

In this project the rate of deformation is sufficiently small for the system to be analyzed under static equilibrium condition

$$\boldsymbol{f_{int}} - \boldsymbol{f_{ext}} = \boldsymbol{0} \tag{2.5.1}$$

and therefore the implicit solver, ABAQUS/Standard will be used. Displacement controlled loading will be applied meaning that the applied loads will be adjusted to maintain the prescribed displacements.

In ABAQUS/Standard, the Static General analysis typically employs Newton's method to solve the nonlinear static equilibrium equation implicitly [1]. This method iteratively computes stresses and strains based on displacements using constitutive equations. These calculated stresses and strains are then compared to the applied loads and boundary conditions to update the nodal displacements. This iterative process continues until the solution converges. For nonlinear problems, each increment usually requires several iterations to achieve a converged solution. The convergence is also dependent on factors such as mesh size and material properties.

Small deformations and an elastoplastic material model will be mainly be considered in this project and ABAQUS/Standard Static General providing solutions at static equilibrium implicitly will be employed.

3   Method- From Paperboard to RVE

The process of transitioning from a physical paperboard to a virtual finite element (FE) model is presented. The process consists of image aquisition, voxel based meshing, assigning material orientations to the elements and calibration of anisotropic material properties. Moreover, a sensitivity study is performed to analyze the effects of volume size and image resolution.

3.1   Image Acquisition and Analysis

Images for analysis are acquired with a X-ray Tomograph Phoenix Nanotome M. Three samples are created by cutting out pieces of the paperboard in MD, CD and 45° as in Figure 6. However, only images from the MD and 45° directions will be used later on. The paperboard used as the basis of analysis in this project consists of 100% softwood fibers.
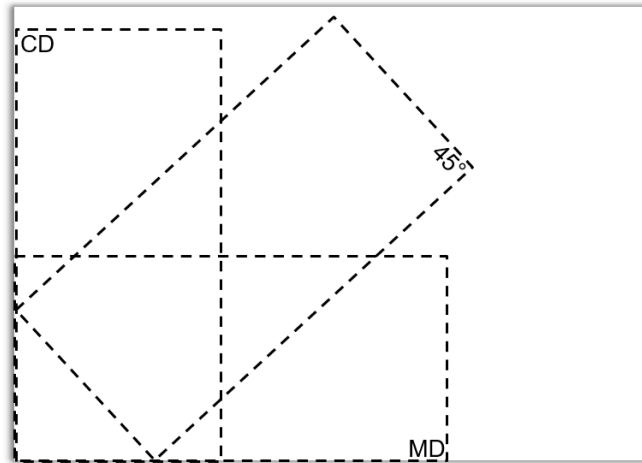
Figure 6: *Samples of paperboard*

All three samples are positioned within a small holder, which is placed onto a rotating stage inside the tomograph. The setup is shown in Figure 7. Care is taken to ensure that the distance between the X-ray source and the sample does not hinder rotation.

Figure 7: *Setup with samples in the industrial nanofocused X-ray CT-scanner Phoenix Nanotome, available at Tetra Pak in Lund.*

Scans with two different pixel sizes, $2\mu m$ and $4\mu m$, are performed. The number of pixels are 3072 in x-direction and 2400 in y-direction, and the distance between the source and the sample controls the size and resolution of the image. By bringing the sample closer to the source, the pixel size decreases while simultaneously reducing the size of the captured area. The settings for image acquisition are presented in Table 4.

Table 4: *Parameter settings on X-ray Tomograph*

Parameter	Value
Timing	500 ms
Average	2
Skip	1
Images	3000
Time	01:27:46 [h:min:s]

Timing represents the time to take one image. Images is the number of images taken for all three samples and corresponds to the number of angles from which the images are taken. Average represents the number of pictures taken at each position, and the final picture is represented by the average of these. To reduce noise and improve image quality, the averaging is set to two. Skip determines the wait interval before a new image is taken at each rotation. When skip is set to 1 it waits 1*timing, i.e the tomograph waits 500ms before taking a picture at each new rotation. Time represents the total time to finalize the image acquisition.

23

The images are imported as Tagged Image File Format (TIF) into the software MATLAB. 214 stacked 2D images are imported for the $4\mu m$ resolution and 321 images for the $2\mu m$ resolution. The voxel intensities are mapped to a 2D- matrix using MATLAB `imread`- function. A lower value of intensity is represented by a darker shade of grey, due to less light hitting the detector. A 3D representation of the sample is reconstructed by stacking the two dimensional images in z-direction, resulting in a three dimensional matrix. The 3D reconstruction of the paperboard with $4\mu m$ pixel size is presented as 2D slices in all planes in Figure 8.
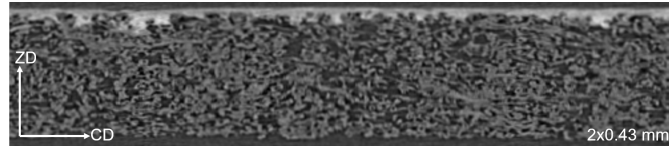
(a) *Slice in XZ-plane.*
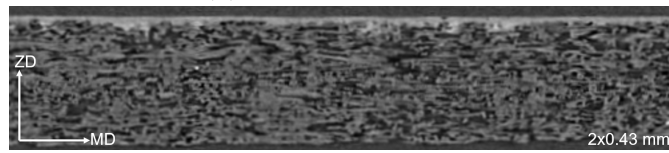
(b) *Slice in YZ-plane.*
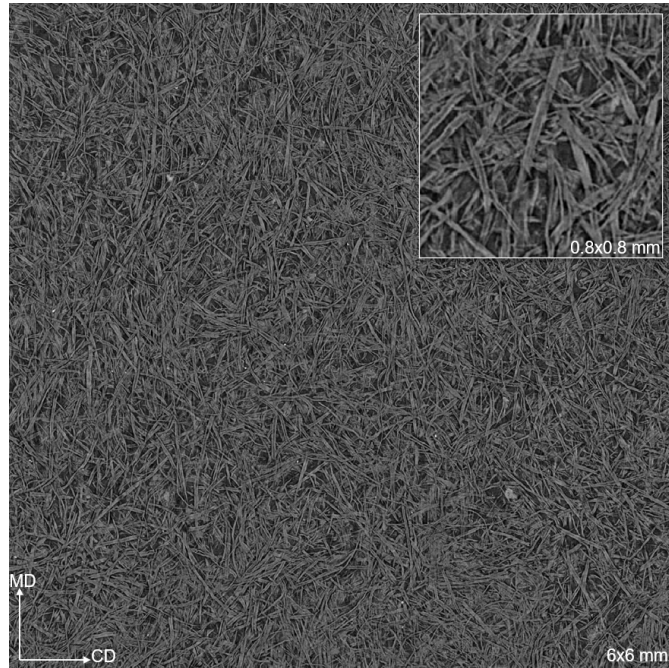
(c) *Slice in XY-plane.*

Figure 8: *Data from X-ray Tomography presented as slices in different planes.*

A histogram of intensity distribution can be plotted. A peak in the histogram may correspond to a phase or constituent in the structure. Otsu's method is used to automatically compute the threshold value used to separate the fibers from the surrounding matrix. The image is binarised by assigning the pixels with a value above the threshold, the value one, and the pixels with values below threshold, the

24

value zero. Segmentation is validated by comparing the mass of the paperboard with an estimation of the total fiber mass of the mesh. The mass fraction is calculated by computing the total weights of the fiber elements in the RVE with the fiber density approximated as 1.5 g/mm^3, against the weight of the scanned paperboard.
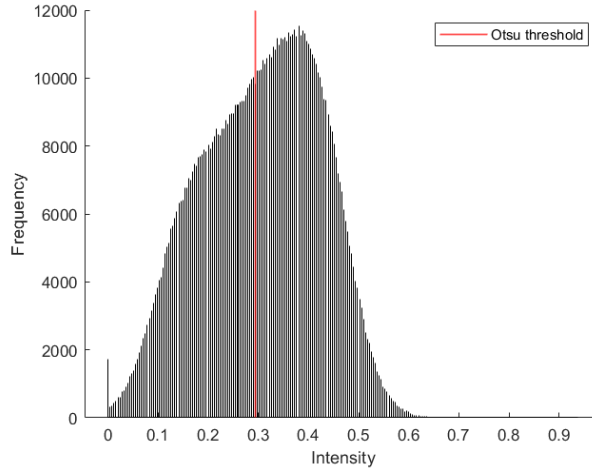

Figure 9: *Histogram of intensities in volume and the Otsu threshold value.*

3.2 Meshing

A voxel based mesh of the volume is created using MATLAB. This is done by mapping image coordinates to nodes and elements as Abaqus inp-file format. Binarisation is performed and element sets are created for fibers and the surrounding matrix. All elements with ones are assumed to be part of fibers, and all elements with zeros are assumed to be air. The voxel based mesh and the element sets obtained from segmentation are presented in Figure 10. In addition to the fiber and void element sets, node sets are created for each side of the volume where boundary conditions will be applied.
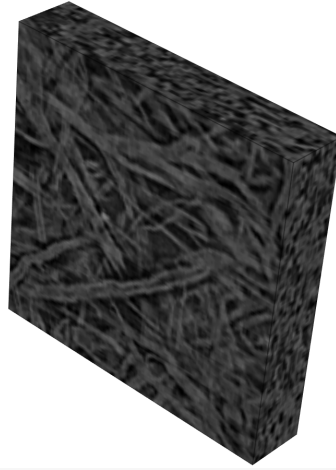
(a) *Reconstructed image of 150x150x30 voxels with MD along horizontal direction.*
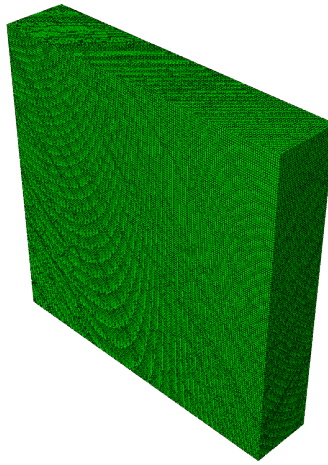
(b) *150x150x30 mesh with element size 4 μm.*
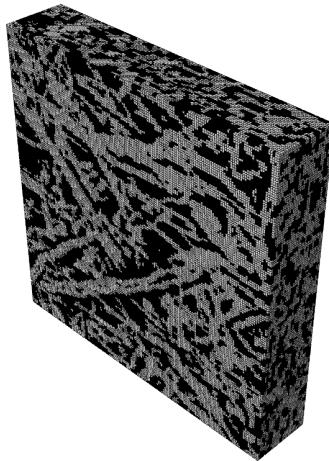
(c) *Fiber and void sets highlighted.*

Figure 10: *Process of creating a finite element mesh and fiber- void element sets.*

3.3 Orientation Study using Structure Tensor Analysis

To produce a finite element model with anisotropic material properties, each element have to be assigned a local material direction. The orientations are calculated using the structure tensor method. Gradients are calculated for each voxel, this is done with both the Gaussian Kernel method and the Abaqus heat flux method. To prevent nonphysical boundaries in the model, the gradients are computed over a larger volume. After the gradient calculations, this volume is cropped to the region of interest, and the structure tensor is calculated specifically within this region of interest

The Gaussian Kernel derivative is computed for each voxel using equation (2.3.5) where σ defines the standard deviation. The surrounding volume around the averaged voxel is defined by the radius r_σ. The equations of the parameters are given in Table 6 and they are determined in relation to an estimated fiber radius r_f defined in Table 5.

Table 5: *Fiber radius approximation.*

Parameter	Value
r_f	$8.5\mu m$

Table 6: *Parameters included in the gradient calculation using Gaussian Kernel method.*

Parameter	Expression
σ	$\frac{r_f}{\sqrt{2}}$
r_σ	r_f

The other approach for determining the gradients of the intensity field using Abaqus transient heat equation, is also evaluated. To map the intensities as temperatures, a predefined temperature field is created. As the field must be defined at the nodes, an average intensity is computed of the adjacent elements. To make sure that Abaqus solves the intended equation (2.3.11), a transient step of one second is created and the density ρ and specific heat c from equation (2.3.9), are set to one. The relation between the conductivity k and the noise scale σ are set as presented in equation (2.3.25). The input parameters are summarized in Table 7.

Table 7: *Material and step parameters for gradient calculations using Abaqus transient heat equation.*

Parameter	Value
Density, ρ	1
Specific Heat, c	1
Conductivity, k	$\frac{1}{2}\sigma^2 = \frac{1}{4}r_f^2$
Time, t	1
Number of increments	1

To compute the gradients in Abaqus, an input file containing the voxel based mesh with element type DC3D8, a predefined temperature field, a conductive material, and step definition is written and imported to Abaqus CAE. A job is submitted and heat flux vector corresponding to the intensity gradient, is saved as a report (rpt) file. The report file is then imported into MATLAB to be used for the final orientation computation.

The structure tensor is calculated from the gradients for each element within the region of interest with equation (2.3.26). The filter radius r_ρ is set equal to the fiber radius. The standard deviation of the kernel is defined by the integration scale ρ and the volume considered is determined by the filter radius r_ρ .

Table 8: *Parameters included in the orientation analysis.*

Parameter	Expression
ρ	$2\sigma = \sqrt{2}r_f$
r_ρ	r_f

The filtering parameters in Tables 6 and 8 are validated based on the accuracy of the gradients and orientations. This is first done by creating fibers in MATLAB. The fibers are placed in different directions, diagonally, and crossing each other to understand the influence of the parameters. One example of a created fiber is presented in appendix (section 6.2). When the algorithm accurately captures the fiber directions for the created fiber a test is also performed on a small volume of the real CT-data. The value of σ was suggested by equation (2.3.1) and the value of ρ was chosen as half of what was suggested in (2.3.28). Both of the filtering radius, r_σ and r_ρ, are set equal to the fiber radius to be as small as possible to reduce computation cost but large enough capture intensity change at the fiber boundaries.

When the parameters are validated the structure tensor is computed for each voxel at a larger volume. The eigenvector corresponding to the smallest eigenvalue, considered the fiber longitudinal direction, is written as a discrete orientation field to a Abaqus inp-file. The input file also contains the voxel based mesh with

element type C3D8, the element sets corresponding to fiber- and void elements and the node sets. The input file is then imported to Abaqus to visualize the orientation vectors. The MD/CD ratio is computed and used to ensure that the distribution of the cropped out volume lies within a reasonable range. The ratio is approximation based on considering the ratio of elements with orientation vectors closest to MD and CD respectively.

Figure 11 shows the final results from gradient calculations using Gaussian Kernel filtering and the corresponding fiber orientations.
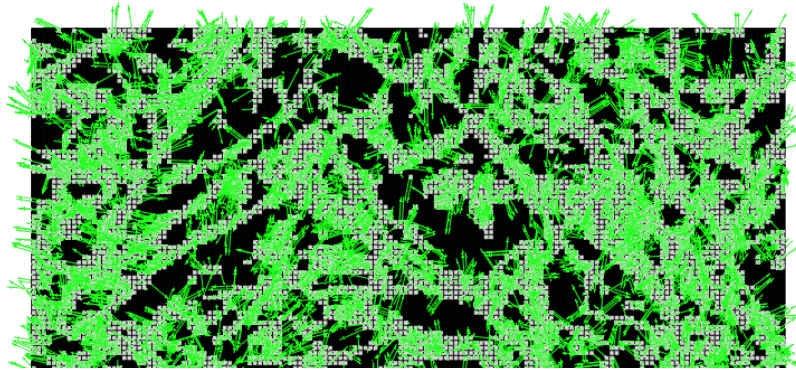
(a) *Intensity gradients.*
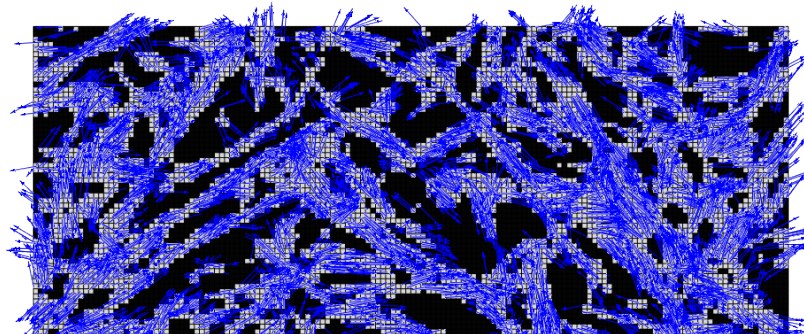
(b) *Fiber orientations*

Figure 11: *Gradients of intensities computed with Gaussian Kernel method, and the corresponding fiber directions for a 2D cut.*

The gradients and orientations for the whole volume are presented in Figure 12. Figure 12c is the final model used for material calibration.
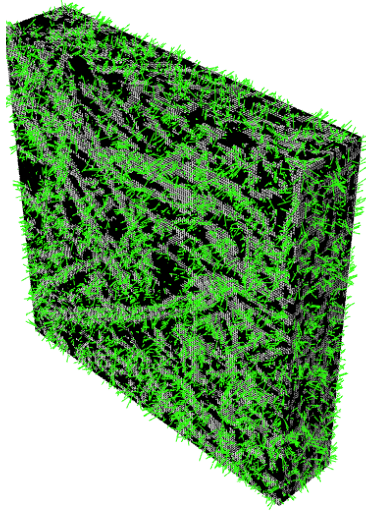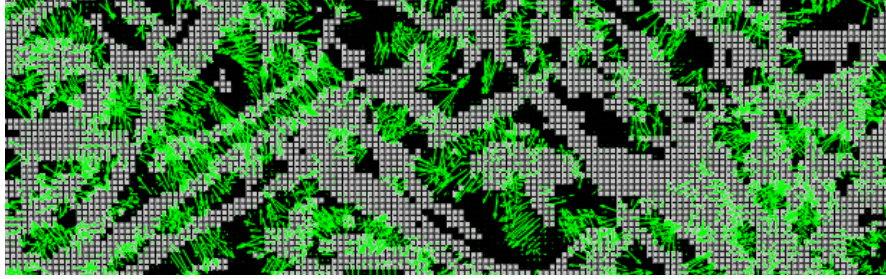
(a) *3D gsradients*
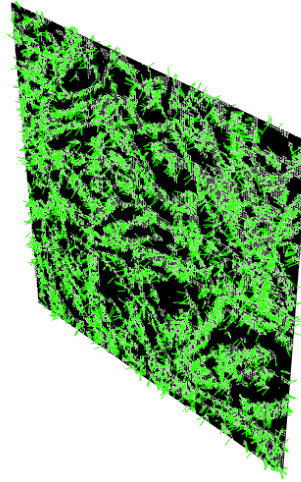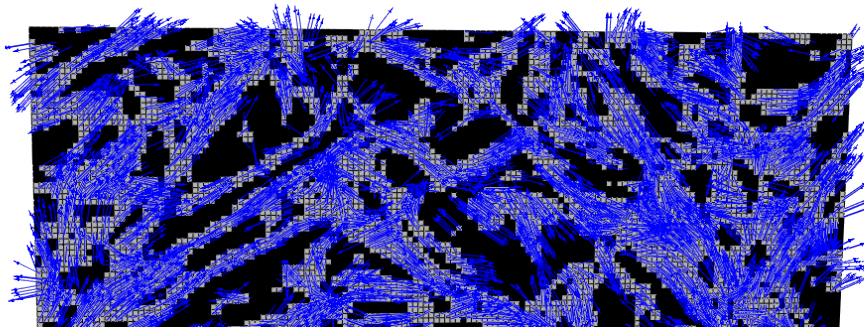
(b) *Gradients, 2D cut*
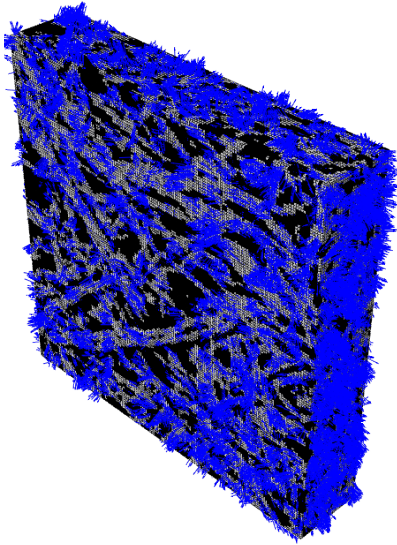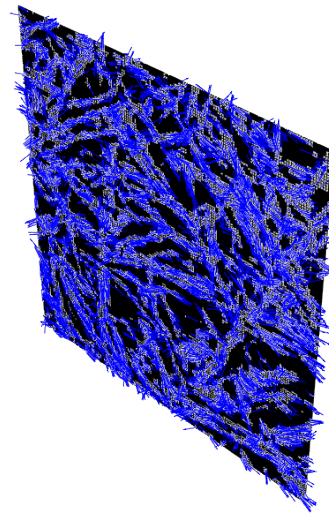
(c) *3D orientations*

(d) *Orientations, 2D cut*

Figure 12: *Gradients of intensities computed with Gaussian Kernel method, and the corresponding fiber directions for full volume.*

The orientations from gradients obtained using Abaqus transient heat equation are presented in Figure 13

30

(a) *Intensity gradients.*

(b) *Fiber orientations.*

Figure 13: *Gradients of intensities using Abaqus heat flux vector and the corresponding fiber direction for a 2D cut.*
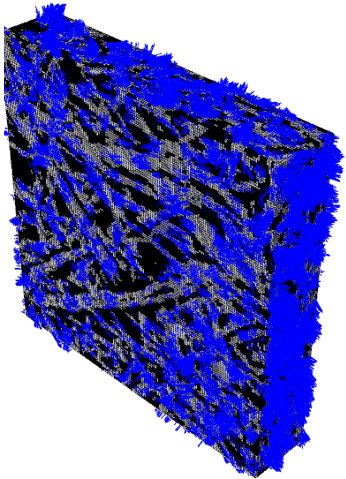
The difference in the gradient plots is mainly due to that in Figure 11a the gradients are plotted as material orientations, while in Figure 13a they are plotted as heat flux vectors. Figure 14 presents the gradients and orientations for the full volume when using Abaqus transient heat equation.
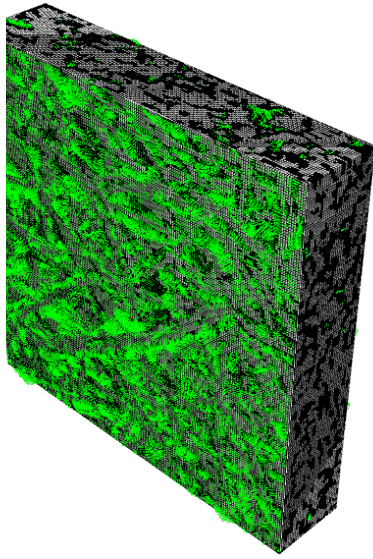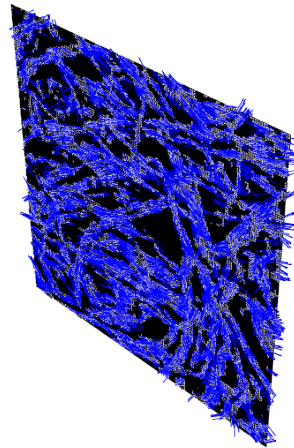
(a) *3D gradients*
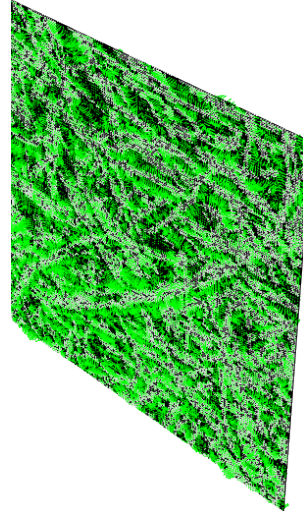
(b) *Gradients, 2D cut*

(c) *3D orientations*

(d) *Orientations, 2D cut*

Figure 14: *Gradients of intensities computed with Abaqus transient heat equation, and the corresponding fiber directions for full volume.*

3.4 Material Calibration

Two different materials are set for the finite element model, following the element set fiber and void subdivision. The void is represented as elastic with a low modulus of elasticity of 10 kPa to closely resemble air. The fibers are mod-

eled as elasto-plastic transversely isotropic and its material parameters are to be calibrated.

The calibration process involves performing two tension test simulations, one in the MD and one in the CD, to calculate the error function. Subsequently, this error is utilized within the Python minimize function to optimize the material parameters. The global response from varying the material parameters is obtained from equations (2.4.3) and (2.4.4), where F is the sum of the reaction forces on the node set subjected to displacement controlled load and ΔL is the displacement. The final parameters are validated against a tension test in 45° direction. The elastic and plastic material calibration are treated separately. Experimental yield points are manually determined and constitute the strain delimiter between the elastic and plastic error computation.

The original experimental data consists of multiple tensile tests in MD, CD and 45° directions. The curves from which the calibration is conducted are chosen manually and are plotted in Figure 15.
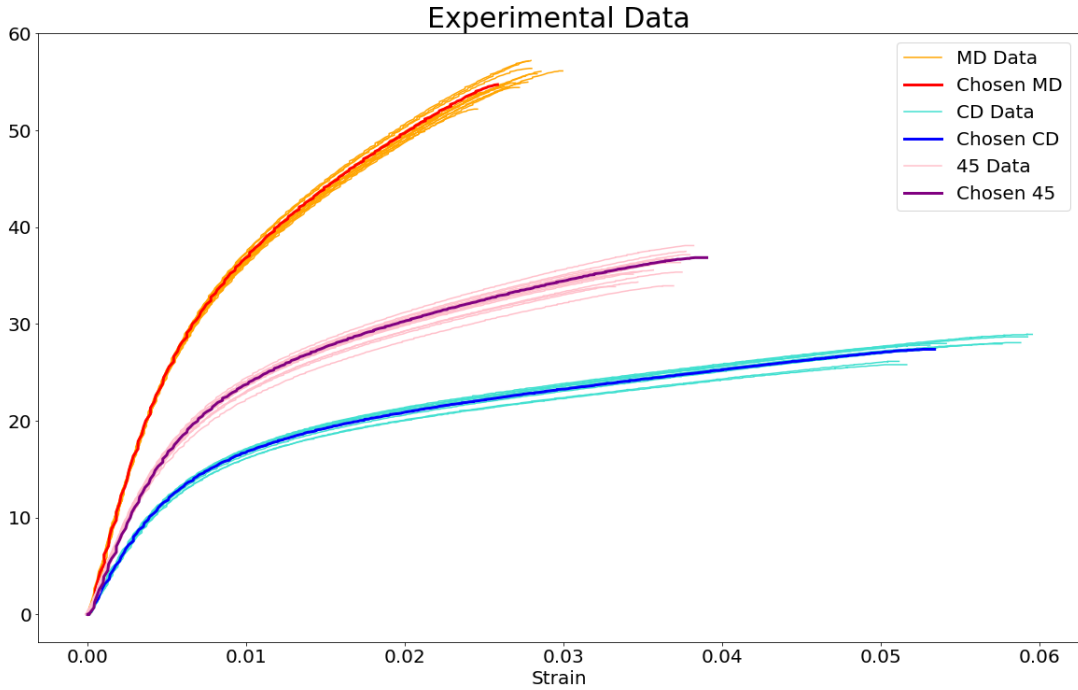

Figure 15: *Experimental data from multiple tensile tests and curves chosen for material calibration.*

3.4.1 Elastic Calibration

Firstly, the elastic modulus, E_L in the fiber direction and E_T in transverse direction, are calibrated to the experimental curve by modelling the fibers as elastic. The error is calculated as the absolute difference between the elastic modulus obtained from the simulated data and the experimental data, both derived from linear regression in the MD and CD directions. Using the Nelder-Mead Simplex

algorithm in Python, iterations are performed to find the elastic modulus resulting in an error considered small enough. E_L and E_T are then set as fix throughout the rest of the calibration process.

3.4.2 Plastic Calibration

The transverse isotropic behavior in the plastic region is defined using the potential parameters (2.4.21) in Hill plasticity model. The yield stress at the corresponding plastic strain is tabulated according to Ramberg-Osgood relation (2.4.30). In the plastic region the error is computed as difference between the interpolated experimental stresses at specified strains.

As the material model is transverse isotropic and 1-direction is considered as the reference direction the three potential parameters to be determined are R_{22}, R_{12} and R_{23}. In equation (2.4.23), these parameters are denoted as R_T, R_{LT} and R_{TT} respectively. From the approximation in equation (2.4.32), R_{23} is calculated, leaving R_{22} and R_{12} as the potential variables to be calibrated.

There are multiple ways to perform the plastic calibration. One of the methods suggested in this report is to first calibrate σ_{y0}, N and E_0 to the MD-curve and then set those values as the initial guess when calibrating MD and CD simultaneously. The other approach is to bypass this step and directly calibrate MD and CD simultaneously. Which method is most time efficient depend on the initial guess. Calibrating MD separately involves setting R_{22} and R_{12} reasonably to accurately represent the relationship between CD and MD. If these parameters are not properly set, the initial guess from the MD simulation may not effectively represent the CD curve in subsequent calibration steps. However, if the initial guess for these values is good, a separate MD calibration can provide a solid starting point for simultaneous calibration in a relatively short time frame.

The efficiency of the simultaneous calibration relies on having a good initial guess for all parameters. However, both methods can operate entirely automatically without requiring manual adjustments, given that the time taken to reach convergence is not a critical factor. The choice between the methods is based on personal preference. A scale factor is also included to determine the order of magnitude that each parameter should be changed during calibration.

3.5 Sensitivity Study

The ability of the calculated orientations to represent the macro characteristics is crucial for ensuring the validity of the model.

A comparison of the two orientation methods is conducted. The gradients computed using Gaussian Kernel filtering is then chosen in further sensitivity studies analyzing the effects of voxel size and model volume to study if the RVE, defined as the smallest volume that effectively captures the macro-level behavior of the paperboard, can be identified. The volumes and voxel sizes studied are presented in Table 9. The volumes in the same column will be used for analyzing impact of volume size, while models in the same row will be used to study the

influence of voxel size. The reference volume that will later be used for material calibration is marked in red.

Table 9: *Volumes that will be used in sensitivity study to analyze the influence of size and resolution.*

Volume size [mm]	$2\mu m$	$4\mu m$	$6\mu m$	$8\mu m$
$0.12x0.12x0.12$		X (27,000)		
$0.16x0.16x0.12$		X (50,000)		
$0.23x0.23x0.12$		X (100,000)		
$0.33x0.33x0.12$	X (1,600,000)	X (200,000)	X (90,000)	X (25,000)
$0.4x0.4x0.12$		X (300,000)	X (97,000)	X (37,500)
$0.52x0.52x0.12$		X (500,000)		
$0.61x0.61x0.12$		X (700,000)		
$0.69x0.69x0.12$		X (900,000)		

3.5.1 Material Orientations and Calibration

The two finite element models obtained from the two image gradient approaches are compared. The ratio of fiber alignment in MD/CD are studied as well as the simulation tensile test response. This is achieved by calibrating the material parameters on the reference volume, obtained with Gaussian Kernel filtered gradients, and then compare the response after applying these same material parameters to the RVE with orientations computed using the Abaqus transient heat equation.

To verify the material, the calibrated parameters are applied to a volume where the fibers are aligned in 45° direction. Important to keep in mind is that the 45° volume comes from a different sample. It is therefore not possible to get the exact same fiber alignment in this test as for the calibrated volume used in MD and CD testing. On the other hand it is possible to make sure that the mass and the orientation ratio are approximately equal.

A simple ideal plastic material model for the fibers is simulated to determine its accuracy in capturing the mechanical behavior of the paperboard, using the potential R_{23} as a variable instead of hardening parameters. Additionally, large deformations are simulated to investigate the differences in results between small and large deformations.

3.5.2 Voxel Size

As reducing the voxel size highly affects the computational cost it is of interest to study at which voxel size a physically plausible result of the model is obtained. To be able to draw a conclusion, different voxel sizes are simulated with constant material parameters. To make sure that the exact same fiber composition is studied, the $2\mu m$ image obtained from the CT-scanning is used as reference. By binning the voxels together using MATLAB `imresize`, lower resolution images can be obtained. The voxel sizes are studied on the volumes $0.33x0.33x0.12$ mm and $0.4x0.4x0.4$ mm as seen Table 9.

3.5.3 RVE Size

Different volume sizes are with constant voxel size, $4\mu m$ are studied. The simulations conducted in the study are given in the column corresponding to $4\mu m$ in Table 9. The volumes are obtained by expanding and shrinking about the same center point. An additional study where the reference volume size is moved to different regions is also performed. The positions examined include volumes located immediately adjacent to the reference volume on the right side and above. It also includes a volume at a random position, further away from the reference volume.

4 Results

Results from the development of a Finite Element Model, material calibration and sensitivity studies are presented in tables and figures.

4.1 FE Model

The final Finite Element Model is presented in the following section. Intensity gradients are computed and fibre orientations are assigned to the elements. In Figures 16 and 17 a cross section of the mesh with gradients computed with the two different filtering methods are presented. Observe that the difference in the gradient plots is mainly due to that in Figure 16, the gradients are plotted as material orientations, while in Figure 17, they are plotted as heat flux vectors. The gradients at the boundaries differ. The gradients plotted as heat flux vectors are plotted over a larger volume, while the Gaussian kernel gradients are plotted within the region of interest. To avoid non-physical boundary conditions the orientations are only determined based on gradients within the regions of interest.
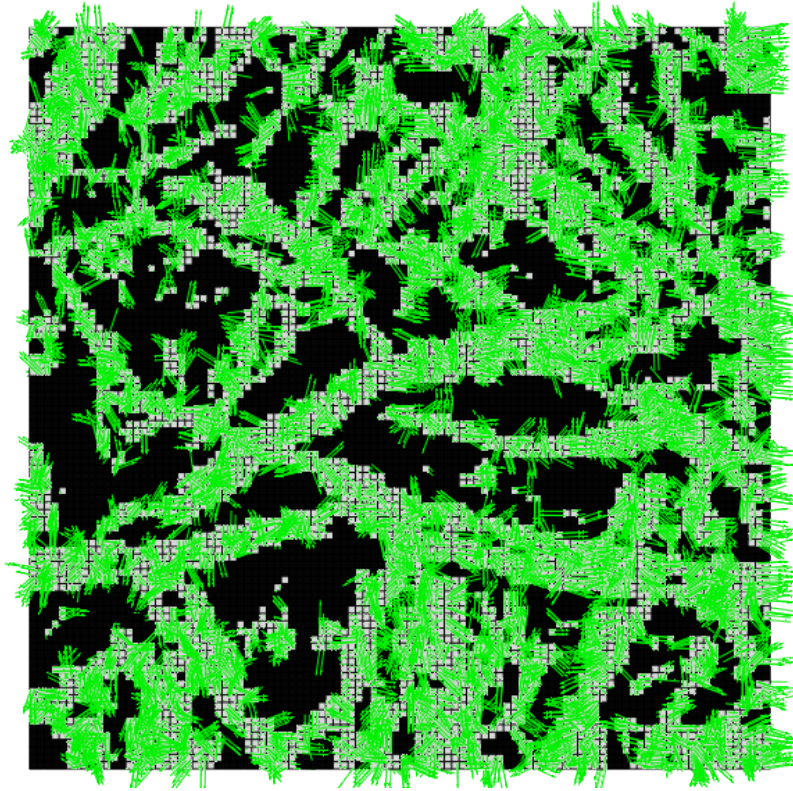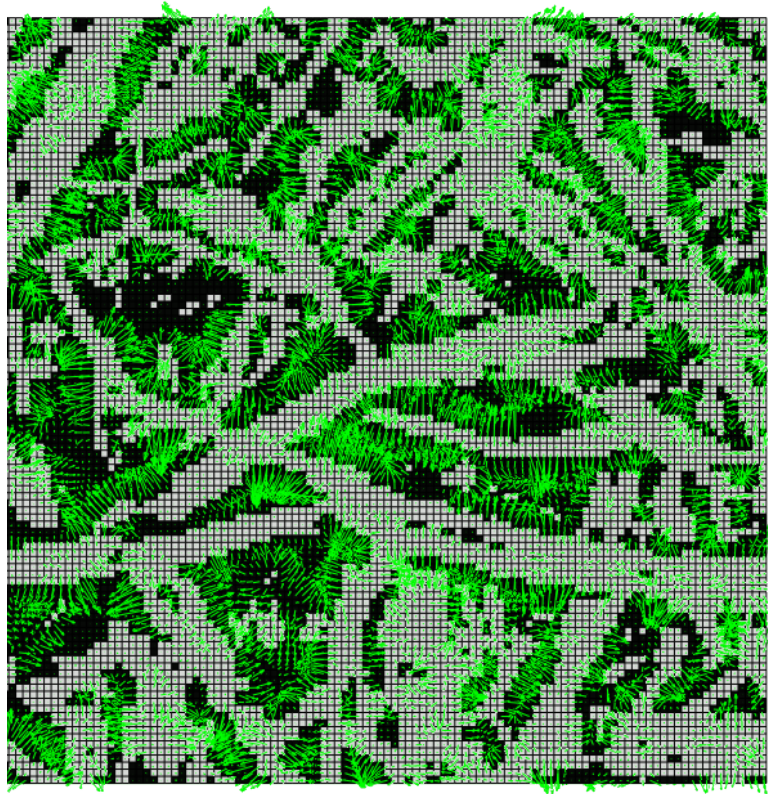
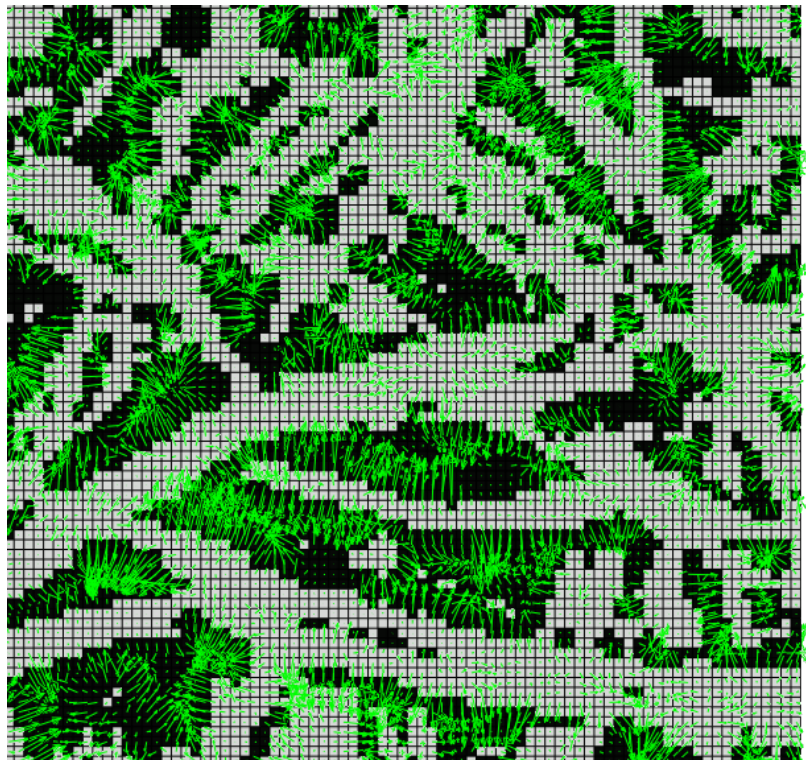(a) *2D cut with Gaussian Kernel gradients.*
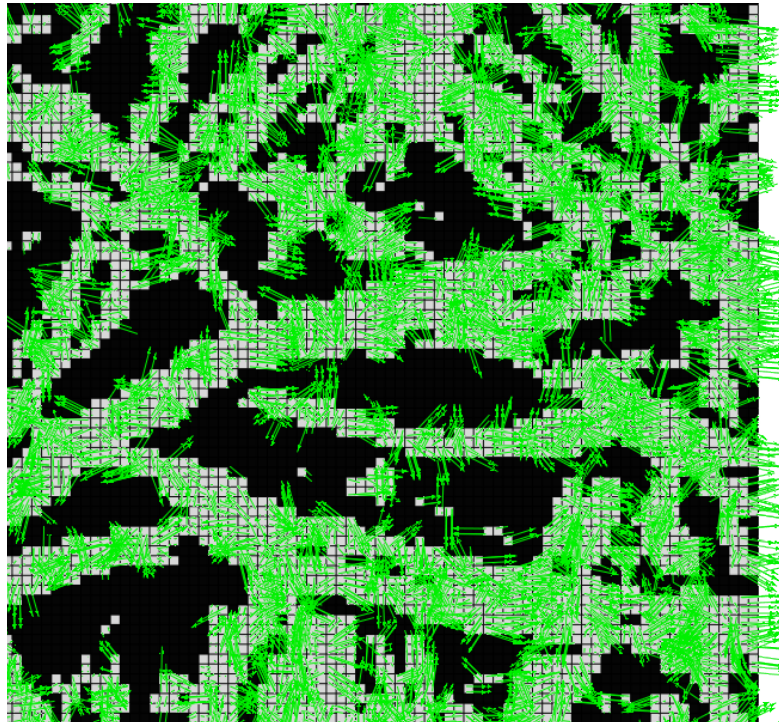
(b) *2D cut zoomed in.*

Figure 16: *Gradients of intensities computed with Gaussian Kernel filtering method.*
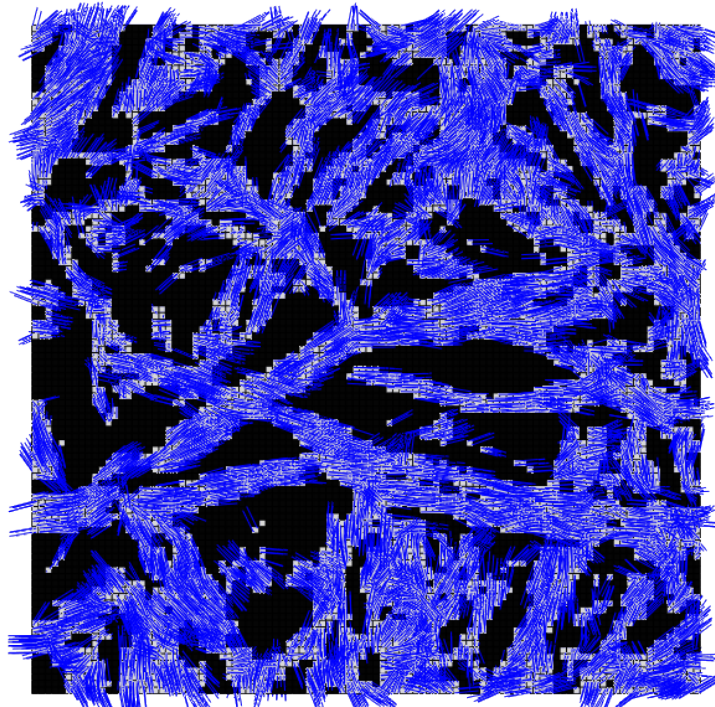
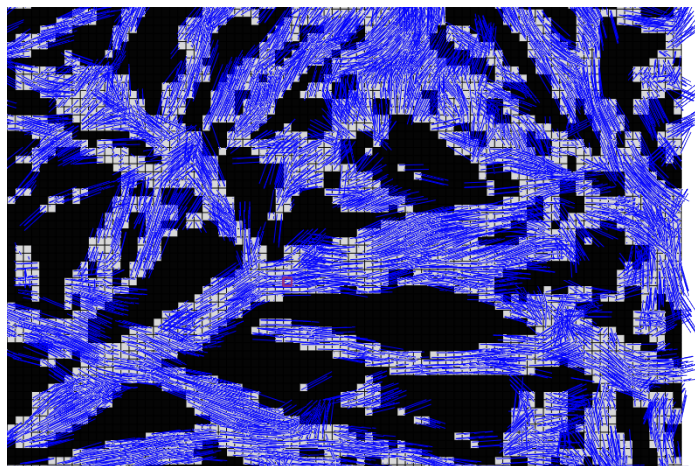(a) *2D cut with Abaqus heat flux gradients.*

(b) *2D cut zoomed in.*

Figure 17: *Gradients of intensities obtained with Abaqus transient heat simulation.*

In Figures 18 and 19, a cross section of the resulting element orientations computed from the different gradients are presented.
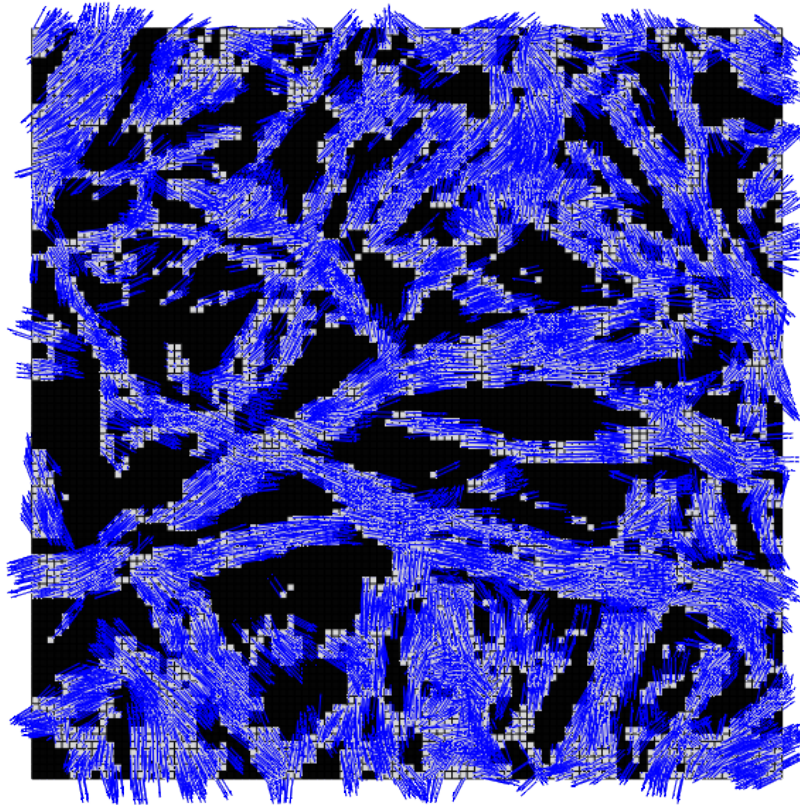

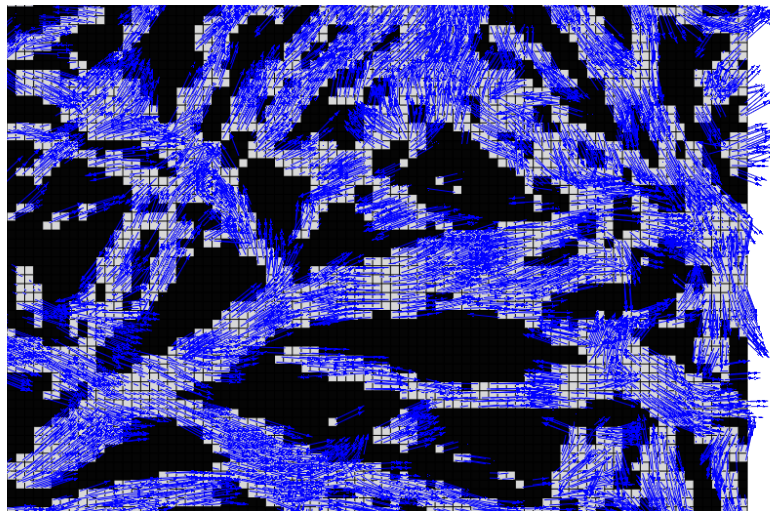(a) *2D cut with orientations from Gaussian Kernel gradients.*

(b) *2D cut zoomed in.*

Figure 18: *Orientations computed from intensity gradients given by Gaussian Kernel filtering method.*

(a) *2D cut with orientations from heat flux vectors.*

(b) *2D cut zoomed in.*

Figure 19: *Orientations computed from intensity gradients given by Abaqus transient heat simulation.*

The orientations observed in the figures appear to be visually almost identical.

4.2 Material Calibration

The reference volume for which the material parameters are calibrated, measures $400x400x120\mu m$ with a pixel size of $4\mu m$, totaling 300,000 elements. The image gradients are computed with Gaussian Kernel method. The simulations are performed with Abaqus Standard- small deformations and element type=C3D8. As a reminder, the mass fraction is calculated by computing the total weights of the fiber elements in the RVE with the fiber density approximated at $1.5g/mm^3$, against the weight of the scanned paperboard. The MD/CD ratio is an approximation based on considering the ratio of elements with orientation vectors closest to MD and CD respectively. Since it is only an approximation, it does not provide detailed information about the precise fiber alignment. The properites on the reference volume are presented in Table 10.

Table 10: *Properties on reference volume used for material calibration.*

Parameter	Measured value
Volume size [mm]	$0.4x0.4x0.12$
Volume size [pixels]	$100x100x30$
Pixel size	$4 \ \mu m$
Number of elements	300,000
MD-CD ratio	$0.62 : 0.38$
Mass fraction	0.9635
Ratio length to fiber radius, δ	47

The final calibrated values are displayed in Table 11 and the corresponding stress-strain curve is presented in Figure 20.

Table 11: *Calibrated material parameters.*

| Parameter	Small deformations
Elastic material parameters	
Elastic modulus, fibers, $E_1 = E_L$	48.4 GPa
Elastic modulus, fibers, $E_2 = E_T$	3.99 GPa
Elastic modulus, air, E_{air}	10 kPa
Poissons ratio, fibres, $\nu_{12} = \nu_{13} = \nu_{23}$	0.3
Poissons ratio, air, ν_{air}	0.3
Plastic material parameters	
Yield stress, σ_{y0}	519.6 MPa
Hardening modulus, E_0	1.98 GPa
Hardening exponent, N	1.25
Potential parameter, R_{12}	0.36
Potential parameter, R_{22}	0.04
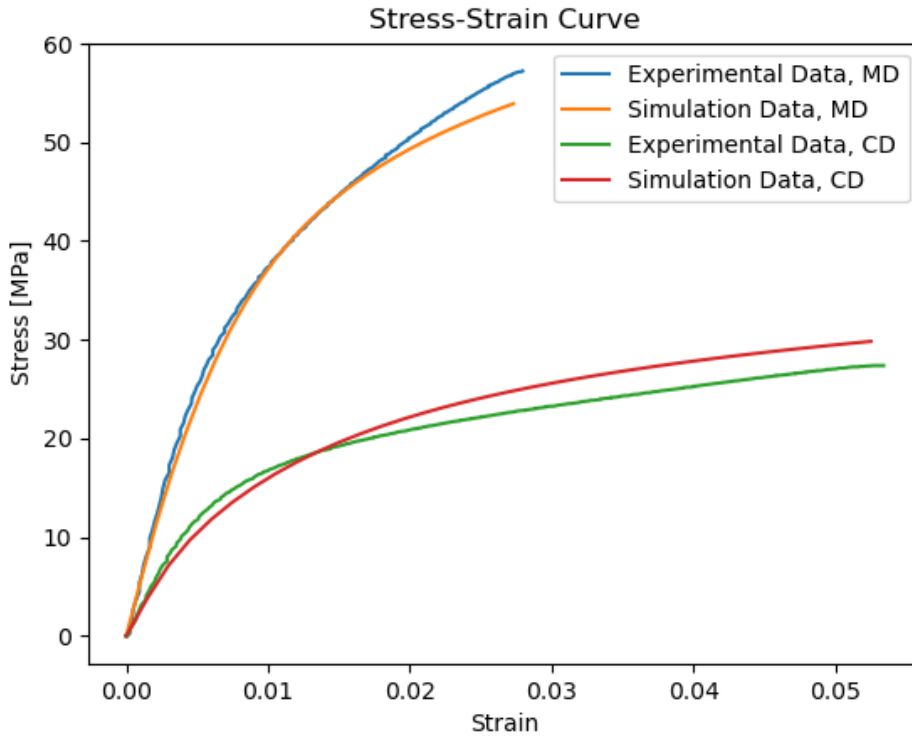
Figure 20: *Stress-strain curves corresponding to the calibrated values presented in Table 11.*
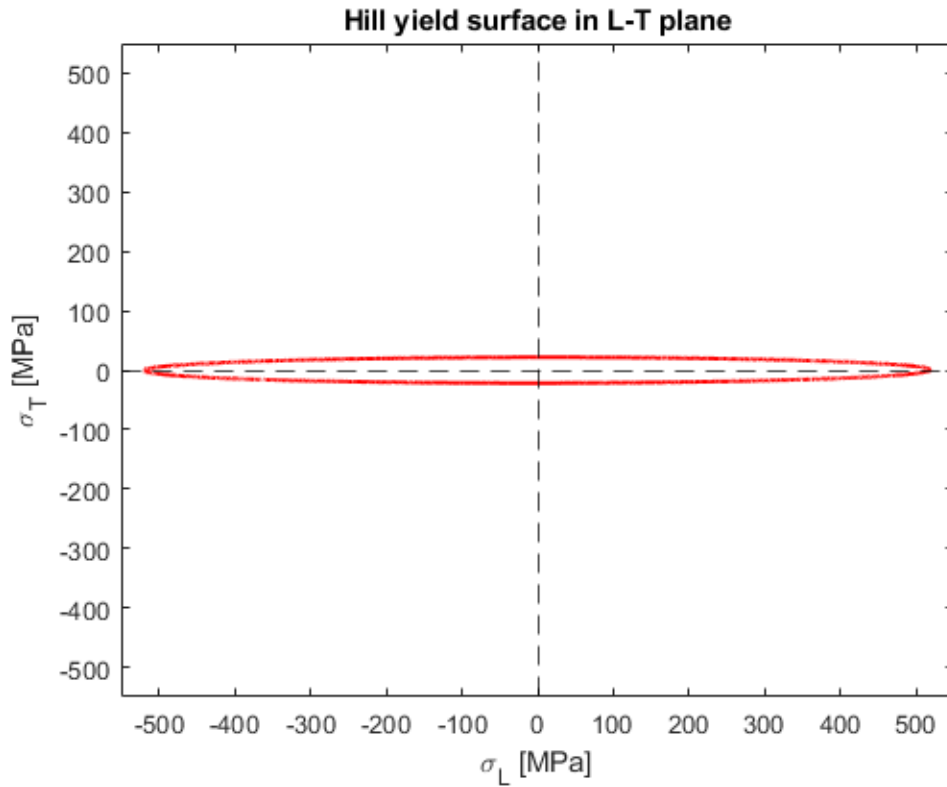
Figure 21: *Hill yield surface in fiber longitudinal-transversal plane.*

Findings:

- The derived material properties indicate a longitudinal elastic modulus of approximately 50 GPa and a transverse elastic modulus of about 4 GPa.

- The elastic modulus in the longitudinal direction is slightly higher than previous findings, in Table 1. The ratio of transverse to longitudinal modulus aligns with a suggested 10% relation found in Table 2.

- The yield strength in the fiber's longitudinal direction is estimated to be around 500 MPa, while in the transverse direction it is approximately 20 MPa.

- The stress-strain curve does not perfectly match experimental data. It can be due to assumptions, initial guess and the chosen material model.

The von Mises stress distributions for a cross section at the maximum strains for both MD and CD are presented in Figures 22 and 23 respectively. von Mises stress does not include anisotropy, but might give an indication of where the higher stresses can be observed.
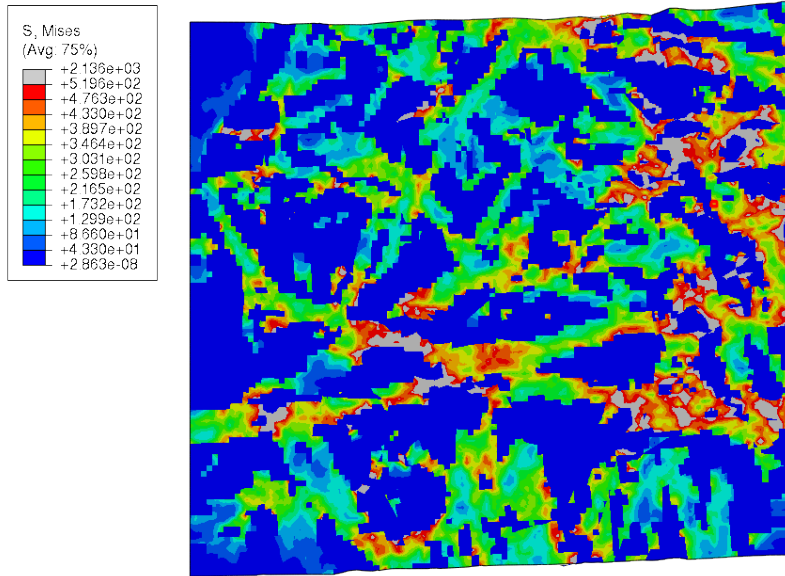
Figure 22: *Stress distribution at the maximum strain of tensile test in MD (horizontal direction). Stresses are given in MPa.*
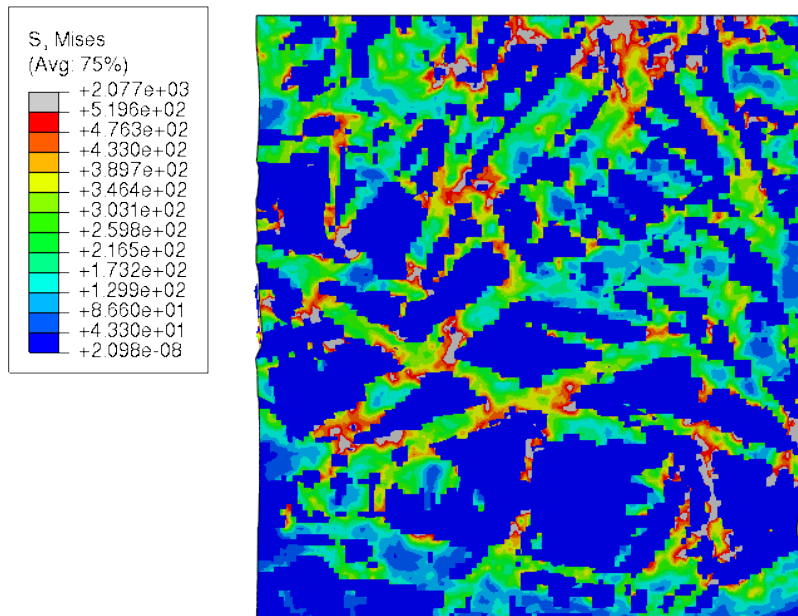

Figure 23: *Stress distribution at the maximum strain of tensile test in CD (vertical direction). Stresses are given in MPa.*

From the figures above it is observed that the model experiences shear stresses and strains. More figures of the whole deformed volume are therefore presented for tensile in MD and CD.
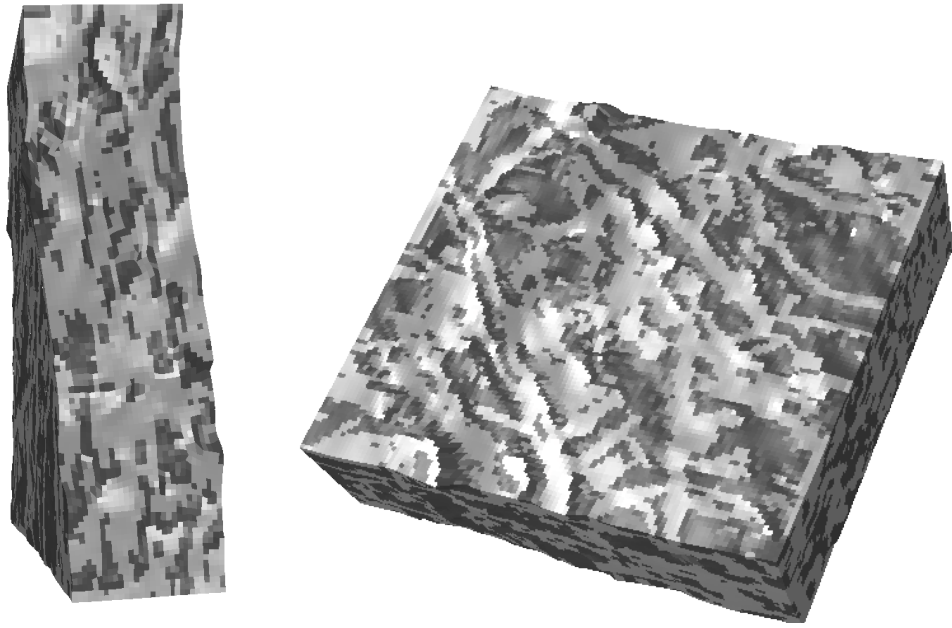
Figure 24: *Deformed volumes from tensile test simulations in MD.*
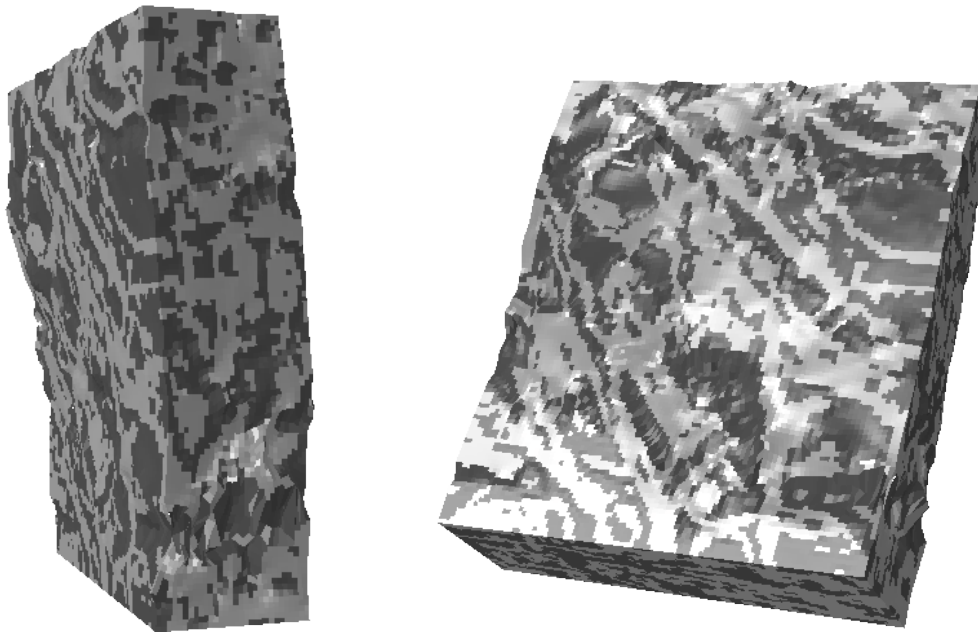

Figure 25: *Deformed volumes from tensile test simulations in CD.*

The stress-strain response for a simulated tensile tests of a single fiber element with calibrated material parameters is presented in Figure 26.
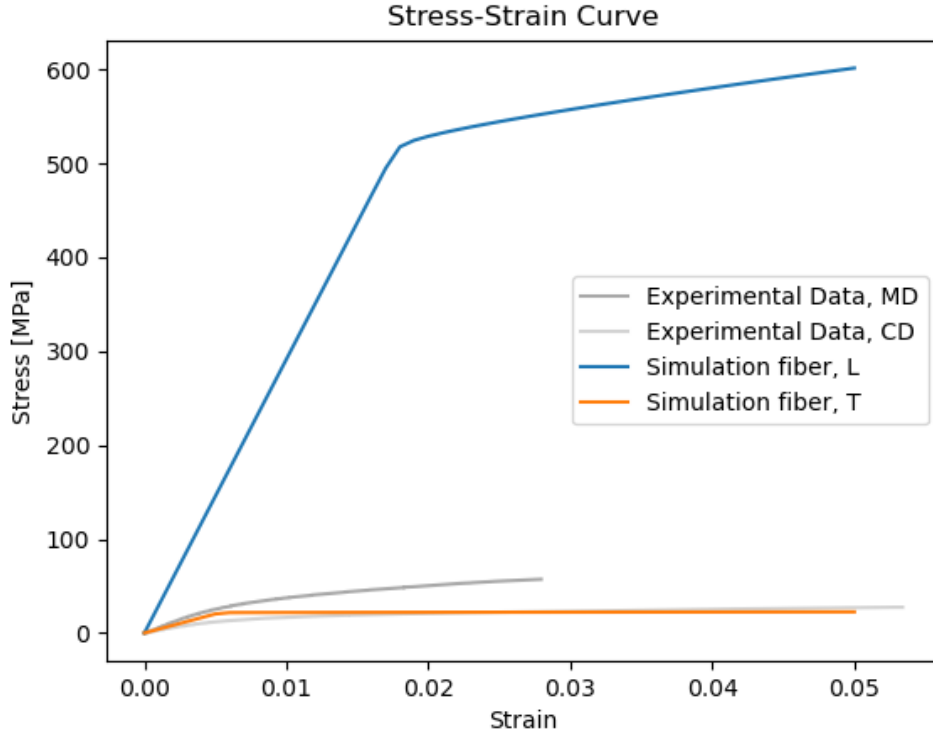
Figure 26: *The blue and orange curves represent the stress-strain response of single fiber tensile simulations in the longitudinal and transverse directions, respectively, using the calibrated values presented in Table 11. The experimental data correspond to experimental tension tests performed on paperboard.*

Findings:

- The longitudinal E-modulus of the fiber is about ten times greater than the paperboard E-modulus in MD, measuring approximately 50GPa and 5.5GPa respectively. In contrast, elastic responses in transverse fiber direction and paperboard CD have closer values, around 4GPa and 2.7GPa, respectively.

In Figure 27 a validation simulation with a 45 degree tension test is presented. Note that the 45 degree sample used for validation was cut out from a different area of the paperboard. MD/CD ratio and mass fraction i therefore used as comparison.

Table 12: *Properties of volumes in MD and 45° image*

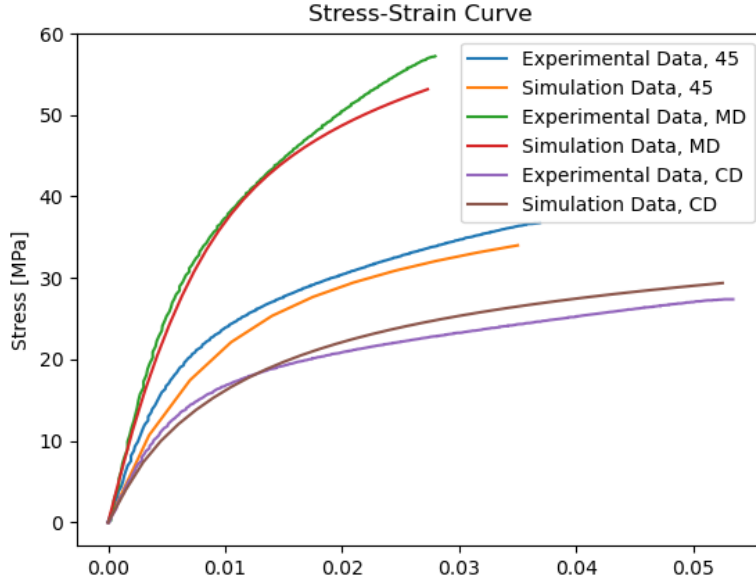| Method	MD-CD ratio	Mass fraction
MD image, Gaussian Kernel gradients	0.60 : 0.38	1.004
45° image, Gaussian Kernel Gradients	0.63 : 0.37	0.9712

Figure 27: *Validation of calibrated material parameters with a with 45° tension test.*

Findings:

- Even though no calibration were performed on 45°, the validation simulation gave a relatively good fit. This suggests that the calibrated parameters are representative for the tested paperboard.

- The results should be interpreted with caution because the 45° test is performed on a different volume and the stress-strain performance is dependent on region of extraction.

4.3 Sensitivity Study

In the following section results from sensitivity studies are presented to examine the impact of the gradient method, volume-size and voxel-size (resolution). The material parameters in the simulations are held constant, as specified in Table 11. The reference image, with 4 μm voxels is used when comparing the gradient methods. When studying volume and resolution a 2 μm image with binning to 4 μm voxel size is the new reference.

4.3.1 Material Orientation

In Figure 28 the resulting stress-strain curves obtained for identical volumes, with orientations computed using Abaqus- heat flux gradients and those computed using Gaussian-Kernel gradients, are shown. The MD/CD ratios are presented in Table 13. As stated in the above section, the ratio is only an approximation to give an indication on the distribution of fibers, it does not provide detailed information about the precise fiber alignment.

Table 13: *MD-CD ratio of orientations computed from the two different gradient methods.*

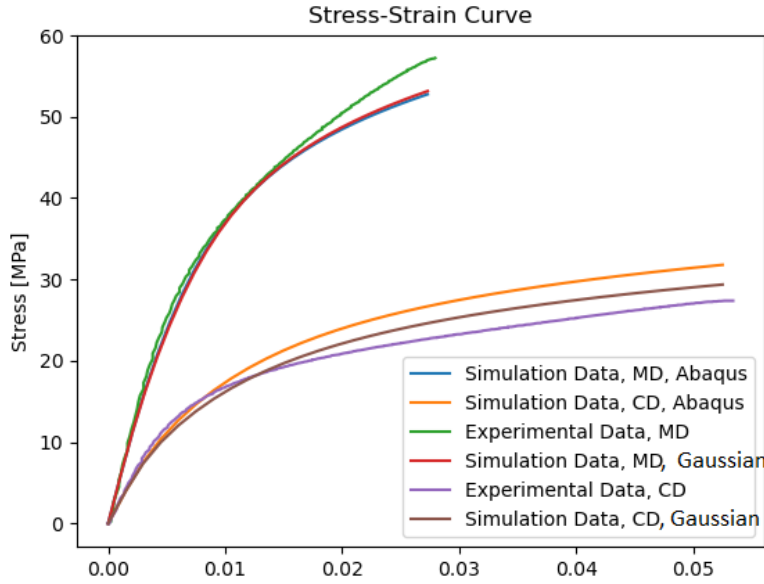| Method	MD-CD ratio
MD image, Gaussian Kernel gradients	0.62 : 0.38
MD image, Abaqus heat equation gradients	0.59: 0.41

Figure 28: *Comparison of stress-strain response when the gradients are computed with Gaussian Kernel filtering method and Abaqus Heat Flux simulations.*

Findings:

- A slight deviation between the orientations and the macromechanical behavior obtained from the different gradient methods is observed.

- The deviation is likely due to the fact that, in establishing the relationship between the filtering parameters (2.3.25), approximations were made leading to a small difference in the final orientation calculations.

4.3.2 Impact of Volume Size

The influence of volume size on the RVE is tested. All volumes have the same centerpoint and thickness, but vary in side lengths. The resolution is kept constant at $4\mu m$. The reference volume for which the material parameters were calibrated is marked in red in the the Table 14. Volume number 1 is the largest volume tested while number 8 is the smallest volume.

Table 14: *Volume sized tested. The reference volume is marked in red.*

Volume	Size [mm]	Resolution	Elements	MD-CD ratio	Mass frac
1	$0.69x0.69x0.12$	4 μm	900.000 ($173x173x30$)	0.60 : 0.40	0.9931
2	$0.61x0.61x0.12$	4 μm	700.000 ($153x253x30$)	0.60 : 0.40	0.9859
3	$0.52x0.52x0.12$	4 μm	500.000 ($129x129x30$)	0.61 : 0.39	0.9923
4	$0.4x0.4x0.12$	4 μm	300.000 ($100x100x30$)	0.62 : 0.38	0.9635
5	$0.33x0.33x0.12$	4 μm	200,000 ($82x82x30$)	0.60 : 0.40	0.9896
6	$0.23x0.23x0.12$	4 μm	100.000 ($58x58x30$)	0.58 : 0.42	0.9927
7	$0.16x0.16x0.12$	4 μm	50,000 ($41x41x30$)	0.53 : 0.47	1.0114
8	$0.12x0.12x0.12$	4 μm	27,000 ($30x30x30$)	0.5 : 0.5	1.0157

The first sensitivity study on size is performed by comparing the response of the reference volume with one smaller (volume 6) and three larger (volume 1-3) volumes.

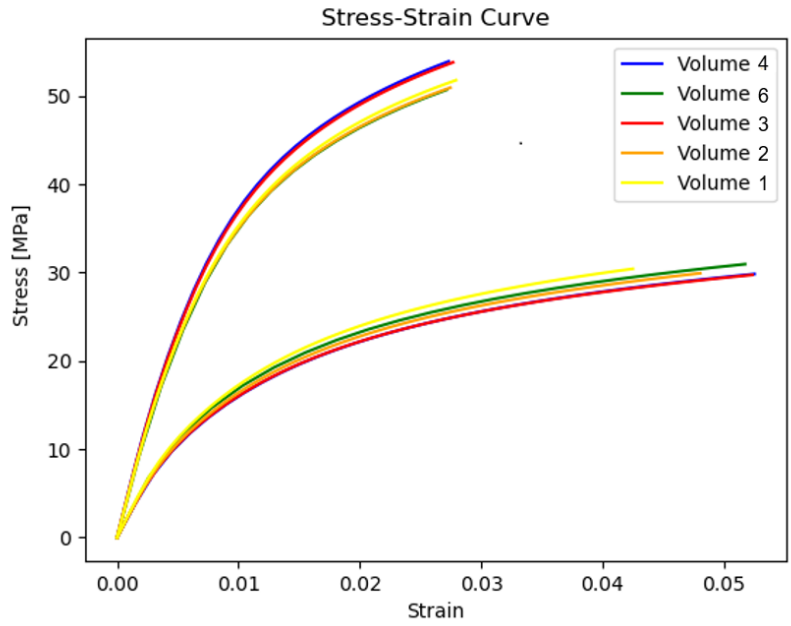Figure 29: *Stress-Strain comparison for volumes larger and smaller than reference volume. Volume sizes are given in Table 14.*

As the response showed no clear dependence on volume size, a similar study comparing the reference volume with only smaller volumes (volume 5-8) is performed.
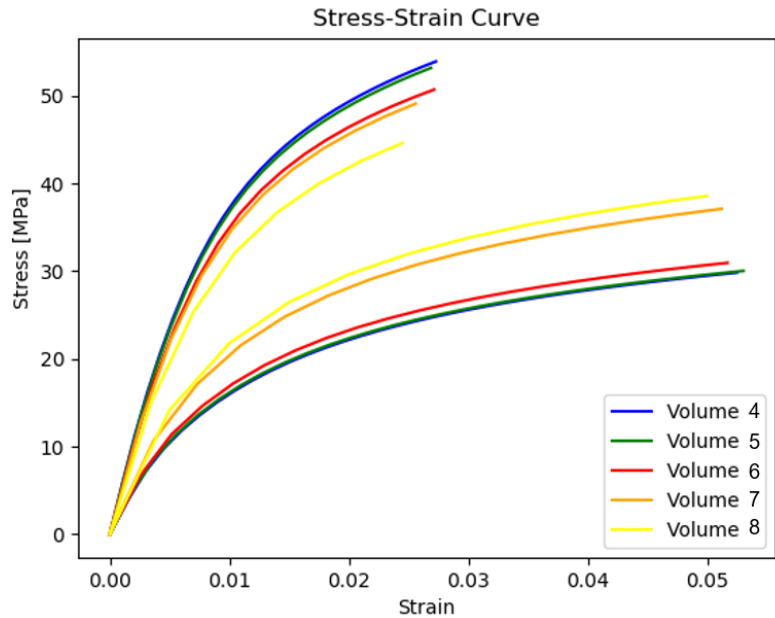

Figure 30: *Stress-Strain comparison for volumes smaller than reference volume. Volume sizes are given in Table 14.*

Findings:

- It is suggested that Volume 5 is a Representative Volume Element for the chosen center point. Volume 5 was the smallest volume to give a response closely aligned with the larger volume's responses.

- To capture the full range of deviation more simulations with volumes extracted from different locations should be performed.

- To truly determine when a volume is representative an acceptable level of deviation in the stress-strain curves should be defined.

Table 15: *Data on volume 5 in Figure 30, which is the smallest volume indicating mechanical representative behavior.*

Parameter	Measured value
Volume size [mm]	$0.33x0.33x0.12$
Volume size [pixels]	$82x82x30$
Pixel size	$4\ \mu m$
Number of elements	200,000
MD-CD ratio	0.60 : 0.40
Mass fraction	0.9896
Ratio length to fiber radius, δ	38.8

Besides maintaining consistent properties as its size increased the RVE- definition also states that the RVE should be independent on the location of extraction. The response from different location of the paperboard is therefore investigated. Volume 4 in Table 14 is used as a reference. Two volumes are extracted from the nearest adjacent locations to the reference volume placement. One volume is positioned directly above the reference placement, and another to its right. The third volume is randomly placed at a further distance from the reference.

Table 16: *Different placements of the reference volume. The positions are given with respect to the reference placement marked in red.*

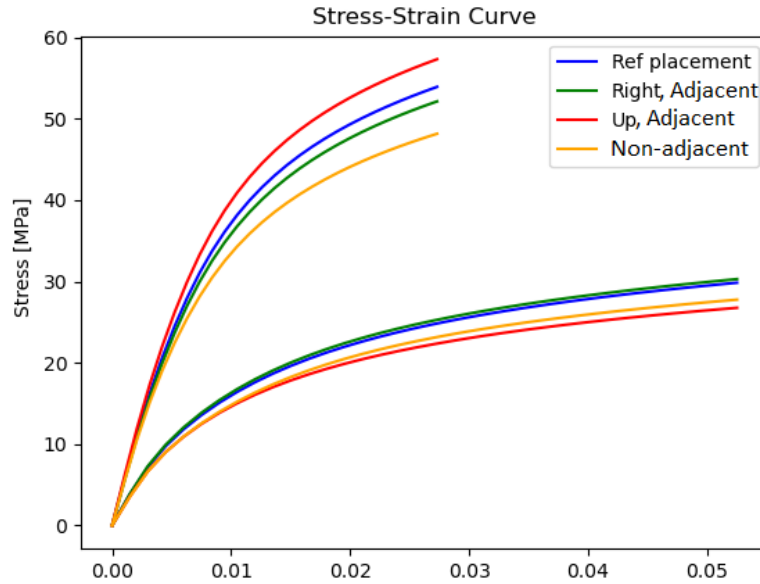| Position	Resolution	Elements	MD-CD ratio	Mass fraction
Reference placement	4 μm	300.000 (100x100x30)	0.62 : 0.38	0.9635
Right (adjacent)	4 μm	300.000 (100x100x30)	0.59 : 0.41	0.9850
Up (adjacent)	4 μm	300.000 (100x100x30)	0.64 : 0.36	0.9750
Non-Adjacent	4 μm	300.000 (100x100x30)	0.63 : 0.37	0.9536

Figure 31: *Volumes 4μm.*

Findings:

- The reference size is dependent on location of extraction.

- Results show that the RVE must be larger than the reference volume (volume 4) to be independent of the location of extraction.

4.3.3 Impact of Voxel Size

In this section the impact of voxel size is explored by studying how a degraded resolution affects the simulated global stress-strain behavior. Volume number 4 with 4μm voxel size is used as the reference. The 2μm resolution is not included in

this comparison as the simulation were found to be too computationally heavy and would have taken several days to complete. The resolutions tested for the reference volume, corresponding number of elements, MD/CD ratio and mass fraction are given in Table 17.

Table 17: *Voxel sizes tested on reference volume size. The reference resolution is marked in red*

Voxel Size	Size [mm]	Elements	MD-CD ratio	Mass fraction
2 μm	-	-	-	-
4 μm	0.4x0.4x0.12	300,000 (100x100x30)	0.62 : 0.38	0.9674
6 μm	0.4x0.4x0.12	97,000 (68x68x21)	0.59 : 0.41	1.0060
8 μm	0.4x0.4x0.12	37,500 (50x50x15)	0.59 : 0.41	1.0225

Images of the same cross section but for the different resolutions are visualized in Figure 32. Stress-strain response from simulating tensile tests on the models are then revealed in Figure 33.
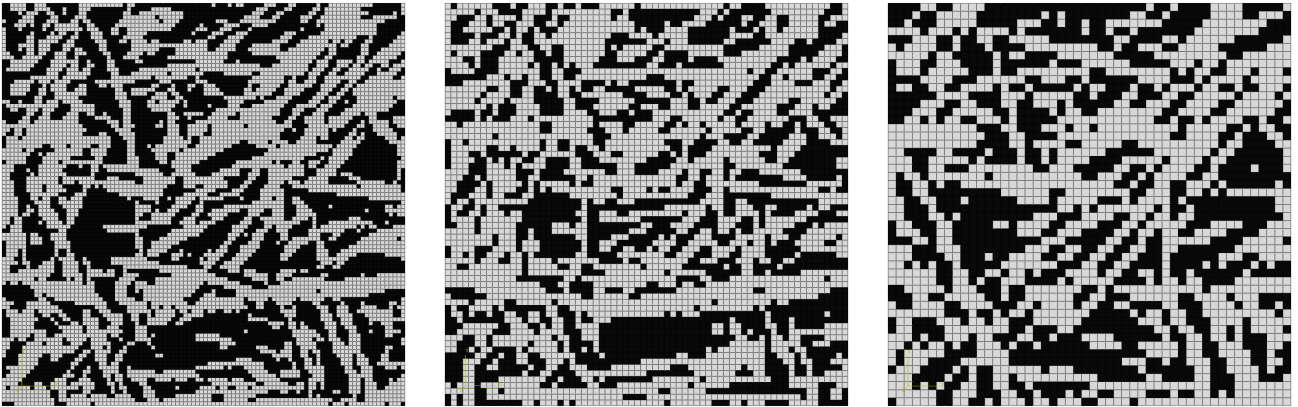

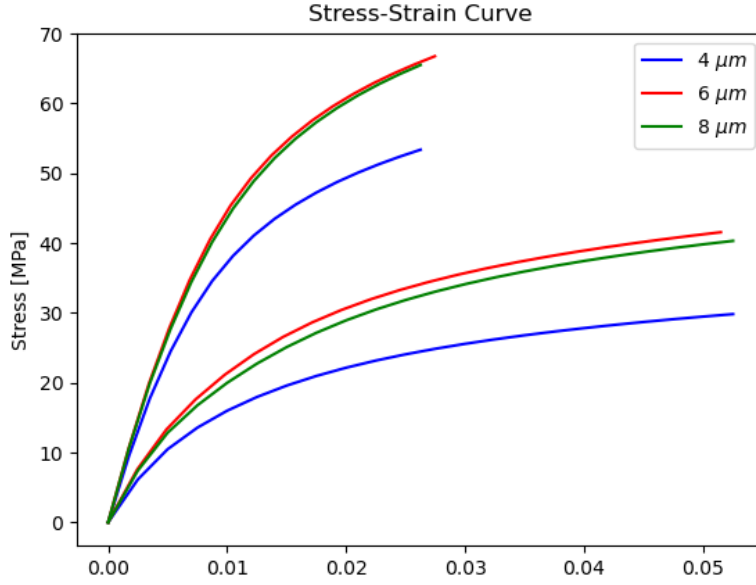Figure 32: *2D cuts of tested volume with resolution 4, 6, and 8 μm.*

Figure 33: *Different resolutions tested on the reference volume.*

To include a $2\mu m$ resolution, the resolutions listed in Table 18 were tested on a smaller volume (volume 5 in Table 14). The images of the cross sections can be found in Figure 34, and the stress-strain response is shown in Figure 35.

Table 18: *Voxel sizes tested on volume 5 in Table 18.*

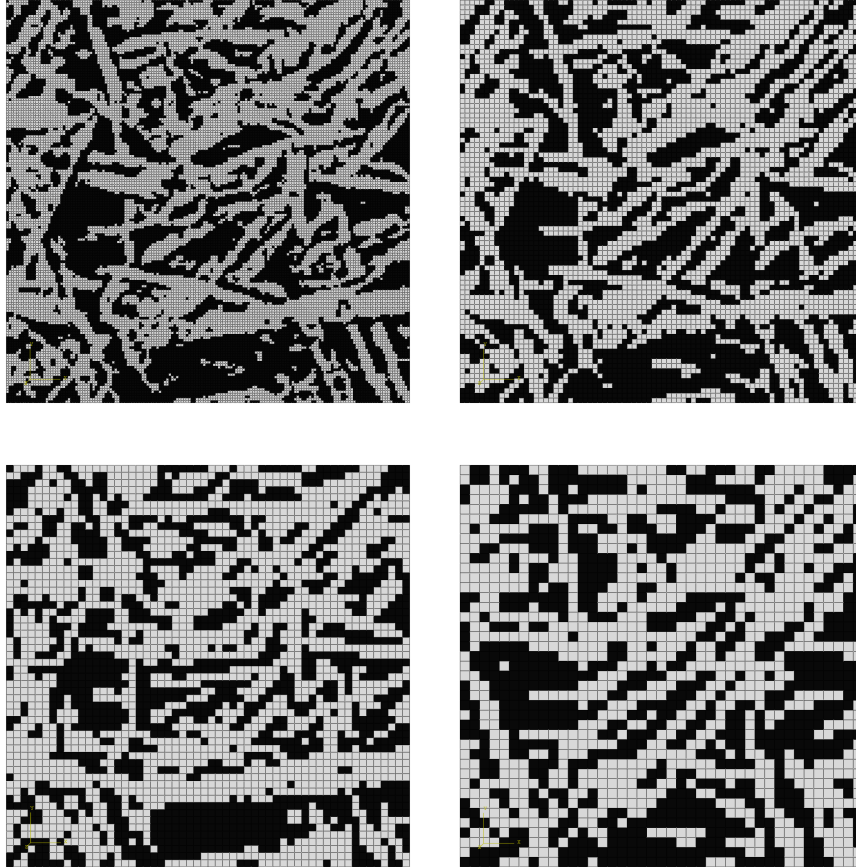| Voxel Size	Size [mm]	Elements	MD-CD ratio	Mass fraction
2 μm	0.33x0.33x0.12	1,600,000 (164x164x60)	0.61 : 0.39	0.9730
4 μm	0.33x0.33x0.12	200,000 (82x82x30)	0.60 : 0.40	0.9896
6 μm	0.33x0.33x0.12	90,000 (60x60x25)	0.58 : 0.42	1.0128
8 μm	0.33x0.33x0.12	25,000 (41x41x15)	0.58 : 0.41	1.0175

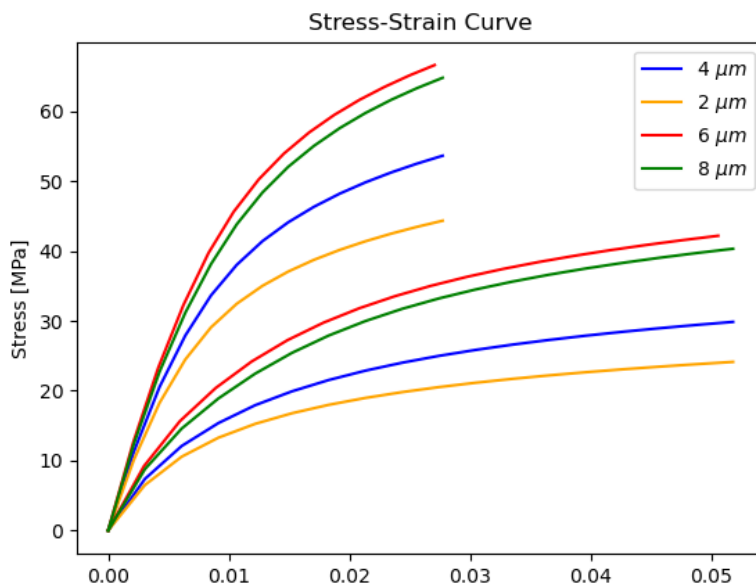Figure 34: *2D cuts of tested volume with resolution 2, 4, 6, and 8 µm.*

Figure 35: *Different resolutions tested on volume 5.*

Findings:

- The resolution of the images significantly affects the response of the RVE.

- The difference between the distinct structures of the 2D cuts in Figure 35 for voxel sizes of $2\mu m$ and $8\mu m$ may be attributed to the binning technique used to achieve lower resolution images or simply to the larger voxel size.

- The resolution highly affects computational time. Computational time for one function call, including two simulations, with 300 thousand elements is approximately 2 hours, while for 1.6 million elements it is three days.

4.4 Material Calibration Large Deformations

After conducting the initial calibration, the optimized parameters presented in Table 11 were utilized as the initial guess for a large deformation simulation. The E-modulus for the air was increased gradually from 0.01MPa until the simulation successfully converged. The E-modulus were then 15MPa. The initial simulation is presented in Figure 36.
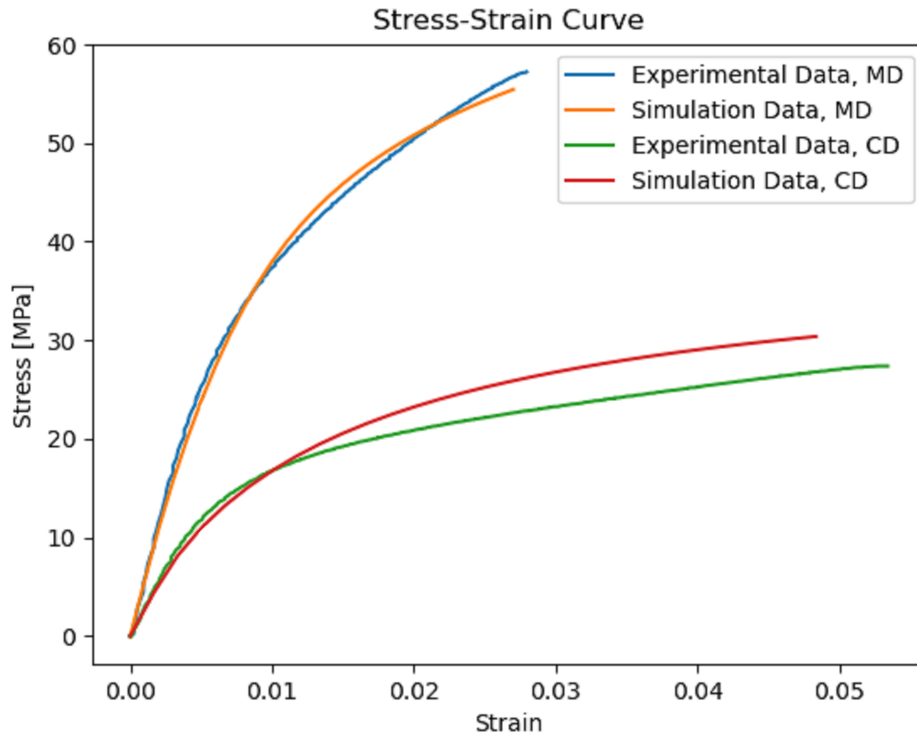

Figure 36: *Intial stress-strain relation for large deformations with $E_{air} = 15 MPa$*

The calibration were then allowed to proceed. The calibrated parameters are presented in Table 19 and the corresponding stress-strain curve is presented in Figure 37.

Table 19: *Calibrated values of material parameters*

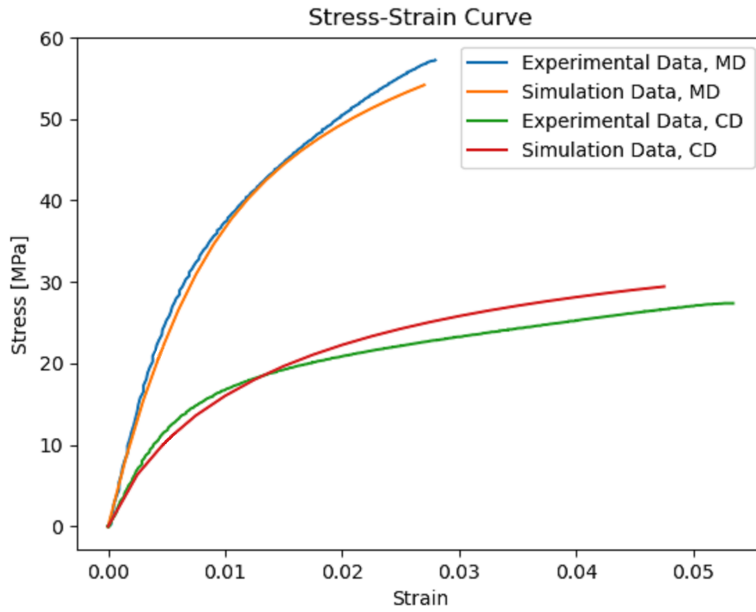| Parameter	Large deformations
Elastic material parameters	
Elastic modulus, fibers, E_L	49.6 GPa
Elastic modulus, fibers, E_T	3.78 GPa
Elastic modulus, air, E_{air}	15 MPa
Poissons ratio, fibres, $\nu_{12} = \nu_{13} = \nu_{23}$	0.3
Poissons ratio, air, ν_{air}	0.3
Plastic material parameters	
Yield stress, σ_{y0}	483.4MPa
Hardening modulus, E_0	2.09 GPa
Hardening exponent, N	1.295
Potential parameter, R_{12}	0.38
Potential parameter, R_{22}	0.04

Figure 37: *Calibrated curve, large deformations with $E_{air} = 15MPa$*

Findings:

- Simulations with large deformations are highly unstable at the current stiffness of air ($E_{air} = 15MPa$). To achieve stability in the calibration, the elastic modulus for air would likely need to be increased further.

- The disparity between the curves in Figure 36, with large deformations, and Figure 20, with small deformations, is minimal. The difference can be both due to increased elastic modulus of air and due to enabling large deformations.

4.5   Material Calibration- Ideal Plasticity

Because the calibrated material parameters with Ramberg-Osgood hardening function, were already optimized to closely approximate ideal plasticity, the decision was made to conduct a simulation using an ideal-plastic material model, with R_{23} treated as a variable. For clarification, while the initial elasto-plastic simulation were conducted with five variable parameters R_{12}, R_{22}, N, E_0, σ_{y0} and R_{23} computed as a function of R_{22}, the ideal- plastic simulations have four variable parameters to be calibrated R_{12}, R_{22}, R_{23}, and σ_{y0}. The initial guess for the ideal plastic simulation were set as the calibrated values presented in Table 20.
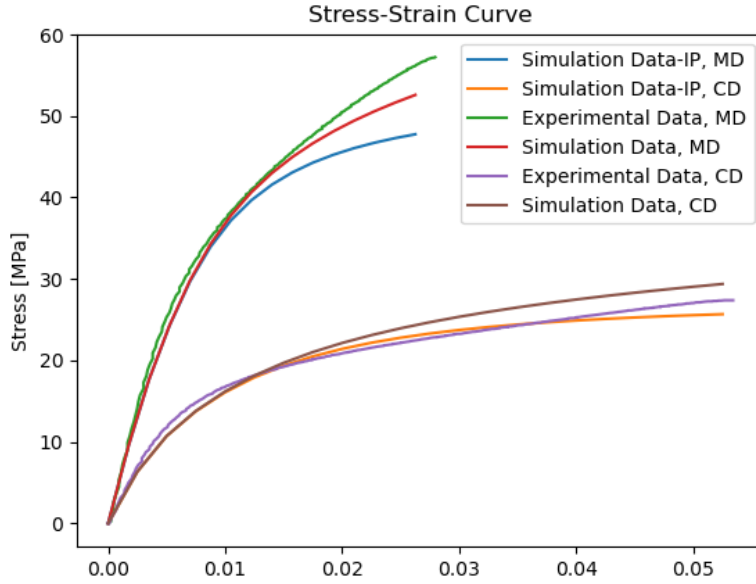

Figure 38: *Comparison of the reference simulation with the initial simulation using a ideal plastic material model.*

The calibration were then allowed to proceed. The final calibrated parameters are presented in Table 20 and the corresponding stress-strain curve is presented in Figure 39.

Table 20: *Calibrated values of material parameters*

Parameter	Small deformations
Elastic material parameters	
Elastic modulus, fibers, E_L	48.4 GPa
Elastic modulus, fibers, E_T	3.99 GPa
Elastic modulus, air, E_{air}	10 kPa
Poissons ratio, fibres, $\nu_{12} = \nu_{13} = \nu_{23}$	0.3
Poissons ratio, air, ν_{air}	0.3
Plastic material parameters	
Yield stress, σ_{y0}	547.5 MPa
Potential parameter, R_{12}	0.41
Potential parameter, R_{22}	0.04
Potential parameter, R_{23}	0.03
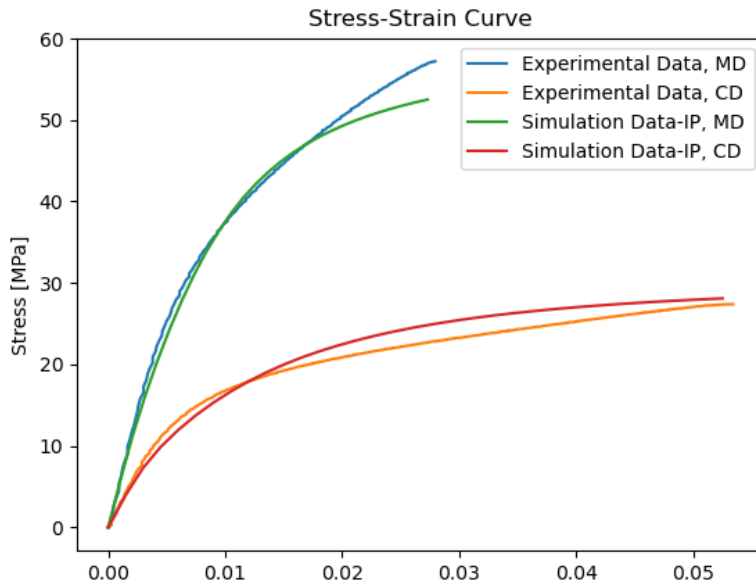
Figure 39: *Calibrated material parameters for fibers with ideal plastic material, with R_{23} treated as a variable.*

Another simulation with ideal plastic material model is performed with the same values of the calibrated parameters as in Figure 39 except for R_{23} that is set to the approximated fixed value used in previous calibrations (equation (2.4.32)). For clarification, the simulations have three variable parameters to be calibrated R_{12}, R_{22}, and σ_{y0}.

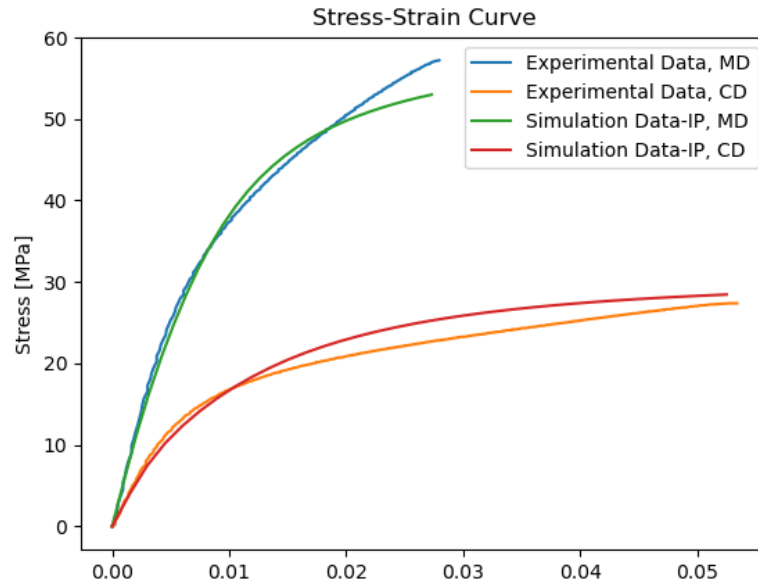Figure 40: *Calibrated material parameters for fibers with ideal plastic material model, with R_{23} approximated.*

Findings:

- The ideal plastic material model has been shown to fit the experimental data very well.

- A minor difference in mechanical response can be observed between calibrating and approximating R_{23}.

- By reducing the number of unknown plastic parameters, time for calibration can be reduced.

5 Conclusion and Future Work

Two methods for computing filtered gradients from a gray scale image have been used. The first method inputs intensities as a predefined temperature field in Abaqus and filter by performing a heat transfer simulation during 1 second. The second filtering method is performed by computing and filtering the gradients with a Gaussian Kernel method. The advantage of using the Abaqus heat flux method is the possibility to visualize the gradients and determine whether the result is reasonable directly in Abaqus CAE. On the other hand, the establishment of a two different inp-files for the gradient and orientation computation, together with the manual work required using Abaqus CAE computing the gradients is not very time efficient. The fact that the Abaqus method requires more manual work, also facilitates the occurrence of errors.

The resulting stress-strain curve comparing the two gradient methods in Figure 28 showed a slight difference. When the establishment of the relation between the filtering parameters (2.3.25) was performed, it was assumed that the Gaussian Kernel integral was calculated over a infinite volume. In the actual computation a limitation radius was chosen and set equal to the fiber radius. The intensity at a point $\boldsymbol{x}$ about a point $\boldsymbol{x_0}$ in space was also approximated by a second order Taylor expansion (2.3.13), leading to a truncation error. Once it was established that the computed orientations only differed slightly, the automatic MATLAB computation was used for all volumes in this project.

Since material parameters are defined locally for the fibers, which can orient in multiple directions, the global MD, CD, and ZD—the calibration process becomes highly complex. Changing one parameter will affect the macro mechanical behavior in both MD and CD. This makes it difficult to use a gradient- based optimization methods without finding local minima. However, using a simplex method (Nelder-Mead was used in this study), with multiple parameters to be optimized, is likely to result in numerous function calls. Besides the number of function calls, the calibration time is also heavily reliant on simulation time and, consequently, the number of elements used.

The primary challenge with the material calibration is the amount of parameters to be calibrated on little data. With five independent parameters calibrated to fit two experimental curves, different combinations can result in similar errors. This makes the calibration very much dependent on the initial guess. However, more work can be put into testing different minimizing algorithms to possibly speed up the convergence. As the calibrated material parameters were optimized to closely approximate ideal plasticity one suggestion to reduce the number of unknowns and speed up convergence is to simulate the fibers as ideal-plastic. Two tests were performed, one where R_{23} was set as variable (Figure 39) and one where R_{23} approximation (equation (2.4.32)) was used (Figure 40). Both calibrations were found to give a relatively good fit to the experimental curves. To truly determine which method is able to give the best fit further calibrations have to be performed. Ideally, R_{23} approximated is good enough and can be used to reduce the number of variables to be optimized, from five parameters (as used in the

62

Ramberg-Osgood model), to three, thereby speeding up the calibration process.

A natural progression in further investigating the micro mechanical behavior on paperboard would be to include fiber bindings into the model. Further investigation is also needed to understand the impact of the parameters that have been approximated and set as dependent in this study. Deeper knowledge in how individual fibers behave and interact may result in a more precise initial guess or an improved plasticity model. The 45 degree validation (Figure 27) can be seen as indication that the approximated parameters used in this study were reasonable.

Even though the macroscopic data of the paperboard can be modelled well using the Ramberg-Osgood relationship and the approximations used in this report, it may be worth investigating whether other material models match the behavior of the fibers better. The main problem with this is that it is difficult to find information on individual fiber characteristics. One example of an approximation that was made in this study was setting the shear modulus G_{TT} equal to G_{LT}. A discussion that occurred was whether or not this was a proper estimation and if it would have been more accurate to set $G_{TT} = \frac{1}{2}G_{LT}$. A simulation with the later mentioned relation was performed and is found in appendix Figure 44 and 45.

The calibration process for large deformations share similar parameters with simulations conducted under small deformations (Table 11 and 19). However, large deformation simulations have challenges due to its reduced stability and sensitiveness to the choice of material parameters, especially the elastic modulus of air. In this study, the elastic modulus of air was increased gradually until the large deformation simulation succeeded. The elastic modulus of air E_{air} is still relatively small compared to the elastic modulus of the fibers (about 300 times smaller than CD and 3000 times less than MD) and did not seem to have a large influence on the material behavior. Further effort is required to achieve model stability when large deformations are enabled, and more studies are necessary to examine how the structure is influenced by large deformations. Our findings suggest that it is advantageous to initially calibrate with small deformations enabled, and then activate the large deformation setting and fine- tune the parameters to reduce the risk of simulation errors during calibration.

Results from investigating the influence of volume sizes, presented in Figure 29, show a minor dependency. Another comparison with smaller volume sizes is therefore performed. Results from Figure 30 show that volume number 5 is the smallest volume indicating representative mechanical behavior. The ratio of length to fiber radius δ for volume 5 is 38.8, and falls within the same range as the values used in previous studies, presented in Table 3. Calculating the exact number of fibers using this voxel-based approach is difficult since the fibers are not distinctly separated. However, a rough estimate suggests there are around 150-250 fibers, which is relatively high compared to the values from previous studies.

The definition of an RVE is, apart from being size independent, that it should be statistically independent of the location from which the sample is extracted. The results from Figure 31 show that the paperboard is inhomogeneous on the scale investigated in this report. The RVE must be larger than the reference volume (volume 4) to capture statistically representative properties, and be independent

on location of extraction. If the material is highly inhomogeneous, a large volume is needed which will lead to heavy computations. However, if the goal is to capture local material characteristics, expanding and contracting around the same central point can be enough to establish the required RVE size. Result in Figure 30 show that volume 5 is large enough to be considered an RVE for the current point of extraction. Moreover, the acceptable level of deviation in the stress-strain should be defined to determine when the volume is truly representative.

Two different volumes were employed to investigate the impact of voxel size. The results are found in Figures 32 and 34. The findings indicate that resolution significantly influences the RVE. In order to conduct tension tests on identical volumes with varying resolutions, image quality was adjusted by binning the voxels from the original 2 μm scans using MATLAB `imresize` function. However, the 2D cross-sectional representations of the binned images do not indicate identical structures (Figure 32 and 34) , particularly noticeable with the 8 μm resolution. To further explore the influence on voxel-size, the influence of voxel-sizes should be examined by scanning the exact same volume, with different resolutions, rather than using binning- techniques. Although two scanning resolutions were available (2 μm and 4 μm), there were some challenges with accurately cropping the exact regions of interest from the stacks, why the decision was made to resize the image in the region of interest using MATLAB.

Results from the 4μm resolution volumes show that the Young's modulus of fibers in the longitudinal direction E_F is approximately 50 GPa, slightly higher than findings from previous studies (Table 3) but still within the same order of magnitude. The Young's modulus in the transverse direction, E_T, is about 4 GPa. This aligns well with the assumption that the elastic modulus in the transverse direction is typically modeled as 10 percent of the elastic modulus in the longitudinal direction. Paperboard consists of fibers that have been mixed and stirred during the paper-making process. Our finding shows that the RVE is smaller than a full-length untreated fiber, typically few millimeters long, and therefore the results from uniaxial tensile tests on full-length individual fibers treated differently may not be directly comparable with our results. The same applies to fiber stiffness's that have been estimated based on fiber composites that consists of other fibers or have gone thorough a different process. For the plastic region, it was rather difficult to find information about fiber characteristics. Our simulations produced the best fit when R_{22} was approximately 0.04, suggesting that the fiber undergoes plastic deformation at a lower stress level in the transverse direction.

A continuation of this project would involve including periodic boundary conditions into the RVE, meaning that the RVE is assumed to repeat periodically in all directions. The use of periodic boundary conditions could allow for smaller volumes as a result of mitigating introduction of inconsistencies at the boundaries. With periodic boundary conditions applied, the RVE would represent an infinite material, more closely resembling the bulk of the material. However, due to the already wide scope of this project and the limited time available, combined with our inexperience with Abaqus, we concluded that implementing periodic boundary conditions was not a priority for this project.

References

[1] Simulia, abaqus, 3dexperience user assistance. URL `https://www.3ds.com/support/documentation/user-guides`.

[2] Artificial intelligence for 3d visualization and analysis software. *ThermoFisher SCIENTIFIC.* URL `https://www.thermofisher.com/se/en/home/electron-microscopy/products/software-em-3d-vis/3d-visualization-analysis-software/artificial-intelligence.html`.

[3] Kostiantyn Vasylevskyi Igor Tsukrov Adam Ewert, Borys Drach. Predicting the overall response of an orthogonal 3d woven composite using simulated and tomography-derived geometry. *Composite Structures*, 243:112169, 2020. doi:https://doi.org/10.1016/j.compstruct.2020.112169.

[4] B.Goyal S.Agrawal R.Vig A.Dogra, A.M.Sharma. Filtering techniques eliminate gaussian image noise. *Laser Focus World*, 2020. URL `https://www.laserfocusworld.com/software-accessories/software/article/14173906/filtering-techniques-eliminate-gaussian-image-noise`.

[5] N.K. Balasubramani, B. Zhang, N.T. Chowdhury, A. Mukkavilli, M. Suter, and G.M. Pearce. Micro-mechanical analysis on random rve size and shape in multiscale finite element modelling of unidirectional frp composites. *Composite Structures*, 282:115081, 2022. doi:https://doi.org/10.1016/j.compstruct.2021.115081.

[6] Nancy R. Sottos Behrad Koohbor, Christopher B. Montgomery. Identification of rve length scale in fiber composites via combined optical and sem digital image correlation. *Composites Science and Technology*, 227:109613, 2022. doi:https://doi.org/10.1016/j.compscitech.2022.109613.

[7] E. Borgqvist. Continuum modeling of the mechanical response of paper-based materials. 2016. URL `https://www.lunduniversity.lu.se/lup/publication/f8bbc8c6-d3b3-406c-88d2-0b15bde42f1f`.

[8] M.J.Cordill A. Matković O. Glushko C. Czibula A. Kulachenko C. Teichert U. Hirn C. Czibula, A. Brandberg. The transverse and longitudinal elastic constants of pulp fibers in paper sheets. *Scientific Reports*, 11, 2021. doi:10.1038/s41598-021-01515-9.

[9] M. Fan D. Dai. 1 - wood fibres as reinforcements in natural fibre composites: structure, properties, processing and applications. pages 3–65, 2014. doi:https://doi.org/10.1533/9780857099228.1.3.

[10] A. Doitrand, C. Fagiano, F.-X. Irisarri, and M. Hirsekorn. Comparison between voxel and consistent meso-scale models of woven composites. *Composites Part A: Applied Science and Manufacturing*, 73:143–154, 2015. doi:10.1016/j.compositesa.2015.02.022.

[11] René de Borst Ellen Kuhl, Ekkehard Ramm. *An anisotropic gradient damage model for quasi-brittle materials*, volume 183. 2000. doi:https://doi.org/10.1016/S0045-7825(99)00213-3. URL `https://www.sciencedirect.com/science/article/pii/S0045782599002133`.

[12] S. W. Zucker A. Dobbins Allan L. Iverson B. Kimia A. Tannenbaum J. Weickert, W. Werdegang. Anisotropic diffusion in image processing. 1996. URL `https://www.researchgate.net/publication/202056812_Anisotropic_Diffusion_In_Image_Processing`.

[13] A. Marmottant N. Limodin D. Bernard L. Salvo, M. Suéry. 3d imaging in material science: Application of x-ray tomography. *Comptes Rendus Physique*, 11(9):641–649, 2010. doi:https://doi.org/10.1016/j.crhy.2010.12.003.

[14] Development Engineering Tetra Pak Laurence Mott, Executive Vice President. Making sustainable progress. 2021. URL `https://www.tetrapak.com/about-tetra-pak/stories/innovating-towards-sustainable-food-package`.

[15] S.G. Lekhnitskii. *Anisotropic Plates*. Gordon and Breach Science Publisher, 1968.

[16] Kang Li, Xiaodong Wu, D.Z. Chen, and M. Sonka. Optimal surface segmentation in volumetric images-a graph-theoretic approach. *IEEE Transactions on Pattern Analysis and Machine Intelligence*, 28:119–134, 2006. doi:10.1109/TPAMI.2006.19.

[17] Petri Mäkelä and Sören Östlund. Orthotropic elastic–plastic material model for paper materials. *International Journal of Solids and Structures*, 40:5599–5620, 2003. doi:https://doi.org/10.1016/S0020-7683(03)00318-4.

[18] A. N. Christensen A. B. Dahl L. P. Mikkelsen N. Jeppesen1, V. A. Dahl. Characterization of the fiber orientations in non-chrimp glass fiber reinforced composites using structure tensor. *IOP Conference Series: Materials Science and Engineering*, 942, 2020. doi:10.1088/1757-899X/942/1/012037.

[19] R. Cristian Neagu, E. Kristofer Gamstedt, and Mikael Lindström. Characterization methods for elastic properties of wood fibers from mats for composite materials. *Wood and Fiber Science*, 38:95 – 111, 2006. URL `https://www.scopus.com/inward/record.uri?eid=2-s2.0-33644673173&partnerID=40&md5=2cebc501f4d46a88de2c3fd8919778c7`.

[20] A. B. Dahl A. N. Christensen V. A. Dahl N.Jeppesen, L. P. Mikkelsen. Quantifying effects of manufacturing methods on fiber orientation in unidirectional composites using structure tensor analysis. *Composites Part A: Applied Science and Manufacturing*, 149:106541, 2021. doi:https://doi.org/10.1016/j.compositesa.2021.106541.

[21] N.Otsu. A tlreshold selection method from gray-level histograms. *IEEE TRANSACTIONS ON SYSTREMS, MAN, AND CYBERNETICS, VOL. SMC-9, NO. 1*, pages 62–66, 1979. URL `https://dspace.tul.cz/server/api/core/bitstreams/36abcc1c-cd72-4569-90ed-607017063124/content`.

[22] N. Saabye Ottosen and M. Ristinmaa. *The Mechanics of Constitutive Modeling*. Elsevier Science, 2005. doi:https://doi.org/10.1016/B978-0-08-044606-6.X5000-0.

[23] Kent Persson. Micromechanical modelling of wood and fibre properties. 2000. URL `https://www.byggmek.lth.se/fileadmin/byggnadsmekanik/publications/tvsm1000/web1013.pdf`.

[24] S. Carmignato V. Cnudde D. Grimaldi C.K. Hagen E. Maire E. Manley A. Du Plessis-S.R. Stock P.J. Withers, C. Bouman. X-ray computed tomography. *Nature Reviews Methods Primers*, 1:18, 2021. doi:https://doi.org/10.1038/s43586-021-00015-4.

[25] Fredrik Berthold R. Cristian Neagu, E. Kristofer Gamstedt. Stiffness contribution of various wood fibers to composite materials. *Journal of Composite Materials*, 40, 2006. doi:https://doi.org/10.1177/0021998305055276.

[26] Y. Zhang C.M. Schlepütz C. R. Gomez M. Mehdikhani C. Breite Y. Swolfs P. Villanueva-Perez R. Guo, J. Stubbe. Deep-learning image enhancement and fibre segmentation from time-resolved computed tomography of fibre-reinforced composites. *Composites Science and Technology*, 244:110278, 2023. doi:https://doi.org/10.1016/j.compscitech.2023.110278.

[27] M. Kerschbaumc I. Sergeicheva Y. Swolfsb S. V. Lomov R. Karamova, L. M. Martullib. Micro-ct based structure tensor analysis of fibre orientation in random fibre composites versus high-fidelity fibre identification methods. *Composite Structures*, 235:111818, 2020. doi:https://doi.org/10.1016/j.compstruct.2019.111818.

[28] L. E. Asp B. J. Blinzler R. M. Auenhammer, L. P. Mikkelsen. X-ray tomography based numerical analysis of stress concentrations in non-crimp fabric reinforced composites - assessment of segmentation methods. *IOP Conference Series: Materials Science and Engineering*, 942, 2020. doi:https://doi.org/10.1088/1757-899X/942/1/012038.

[29] L. E. Asp B. J. Blinzler R. M. Auenhammer, L. P. Mikkelsen. Automated x-ray computer tomography segmentation method for finite element analysis of non-crimp fabric reinforced composites. *Composite Structures*, 256:113136, 2021. doi:https://doi.org/10.1016/j.compstruct.2020.113136.

[30] L. P. Mikkelsen V. A. Dahl L. E. Asp B. J. Blinzler R. M. Auenhammer, N. Jeppesen. Robust numerical analysis of fibrous composites from x-ray computed tomography image data enabling low

resolutions. *Composites Science and Technology*, 224:109458, 2022. doi:https://doi.org/10.1016/j.compscitech.2022.109458.

[31] Y. C. Wang P. J. Withers C. Rau A. Parson C. Soutis R. M. Sencu, Z. Yang. Generation of micro-scale finite element models from synchrotron x-ray ct images for multidirectional carbon fibre reinforced composites. *Composites Part A: Applied Science and Manufacturing*, 91:85–95, 2016. doi:http://dx.doi.org/10.1016/j.compositesa.2016.09.010.

[32] E. Verboven S.W.F. Spronk F.A. Gilabert M. Kersemans L. Pyl W. Van Paepegem R.D.B. Sevenois, D. Garoz. Multiscale approach for identification of transverse isotropic carbon fibre properties and prediction of woven elastic properties using ultrasonic identification. *Composites Science and Technology*, 168:160–169, 2018. doi:https://doi.org/10.1016/j.compscitech.2018.09.016.

[33] Jaan-William Simon. A review of recent trends and challenges in computational modeling of paper and paperboard at different scales. *Archives of Computational Methods in Engineering*, 28, 2020. doi:http://dx.doi.org/10.1007/s11831-020-09460-y.

[34] Laurence Mott Stephen Shaler, Les Groom. Mechanical properties of individual southern pine fibers. part ii. comparison of earlywood and latewood fibers with respect to tree height and juvenility. *Wood and Fiber Science*, 2007. URL `https://wfs.swst.org/index.php/wfs/article/view/1753`.

[35] H.K. Versteeg and W. Malalasekera. *An Introduction to Computational Fluid Dynamics*. Pearson Education Limited, 2007.

[36] Torbjörn Wahlström. Prediction of fibre orientation and stiffness distributions in paper – an engineering approach. *Trans. of the XIVth Fund. Res. Symp. Oxford, 2009*, 2009. URL `https://api.semanticscholar.org/CorpusID:201819007`.

6   Appendix

6.1   Workflow

A systematic workflow for going from X-ray scanned images of paperboard to a Finite Element Model including calibrated material properties of fibers are presented. The software used for gradient and orientation computations includes MATLAB and Abaqus, with the use of Abaqus being manual. Material calibration is performed using a Python script that automatically submits jobs to Abaqus.
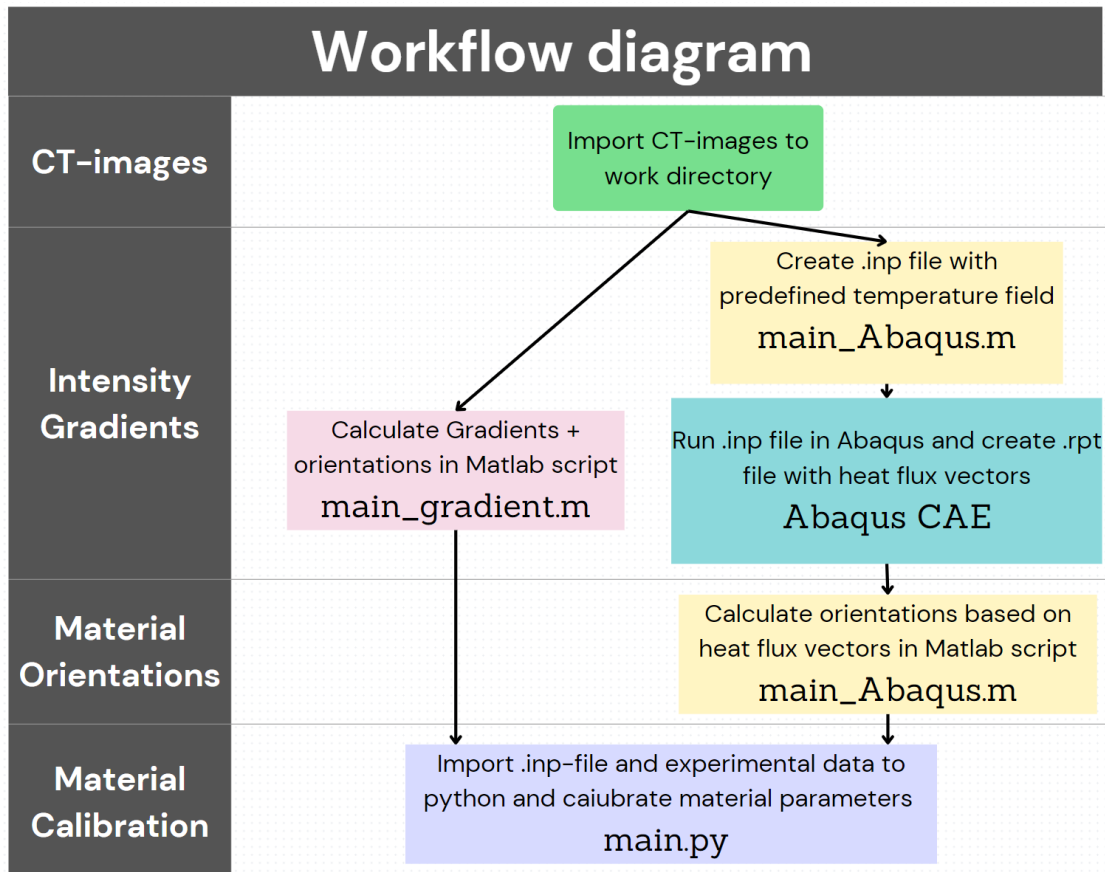

Figure 41: *The overall workflow for transforming X-ray images to a Finite element model*

A more detailed wokflow of the material calibration process is included. The workflow is performed automatically but require manual inputs and decision on whether the optional calibration should be included.
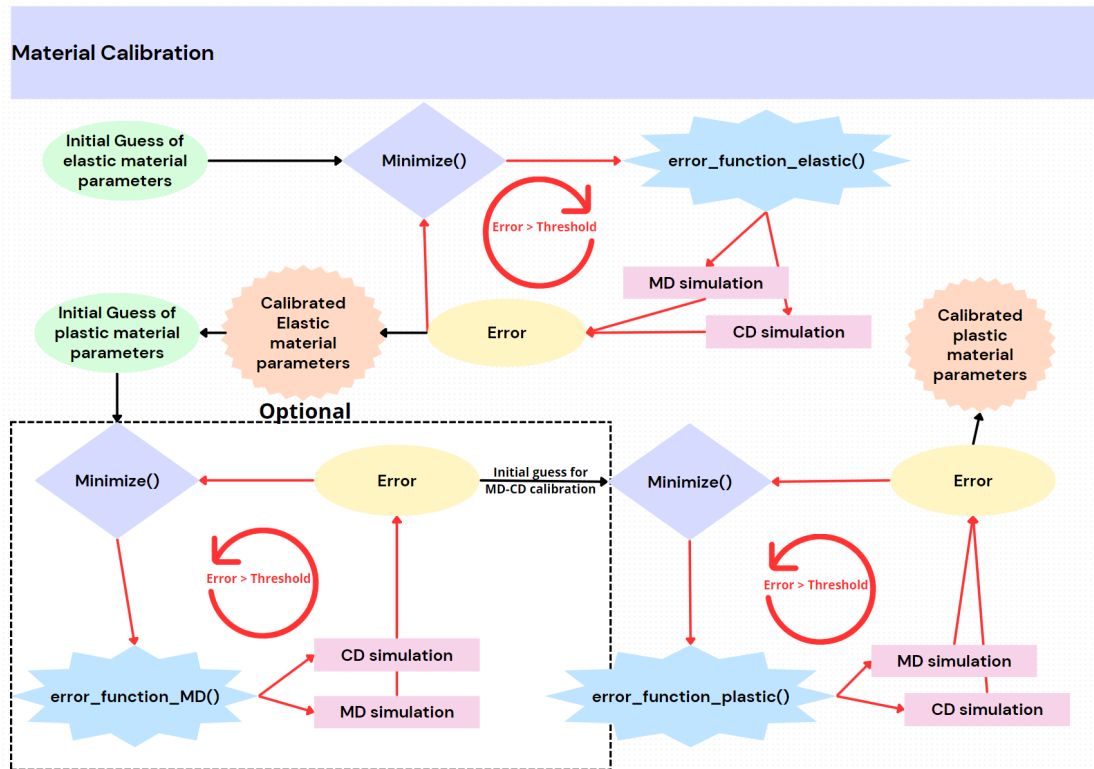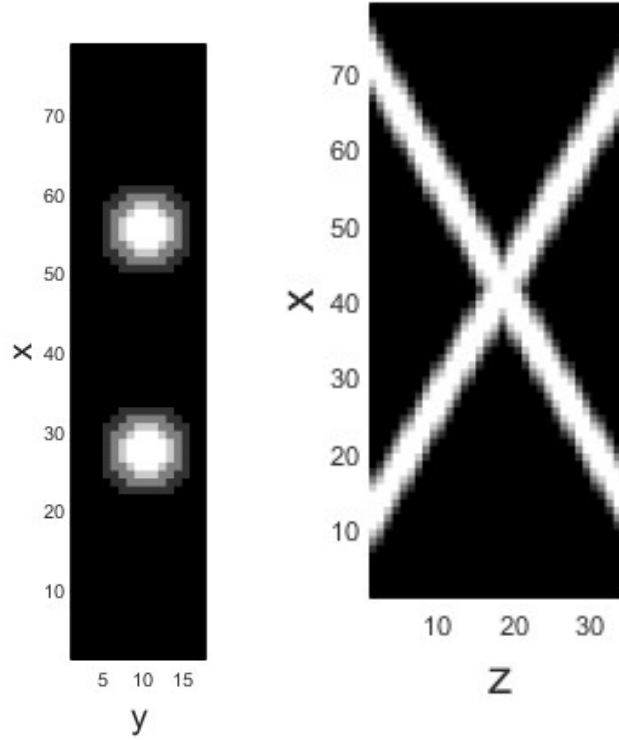
Figure 42: *Process for material calibration*

6.2 Fiber Replication

A fiber replication created with MATLAB and used to validate the effects of parameters used in the orientation analysis.

(a) *Fiber in xy-plane*   (b) *Fiber in xz-plane*

Figure 43: *The created ideal fibre for validating filtering parameters.*

6.3   Effect of Changing Shear Modulus, G_{TT}

A test to analyze the effects of shear modulus estimation, G_{TT}, also denoted G_{23}, was performed. No significant difference was observed when G_{TT} was set to half of what was used in the initial calibration where G_{TT} was set equal to $G_{LT} = G_{12}$.
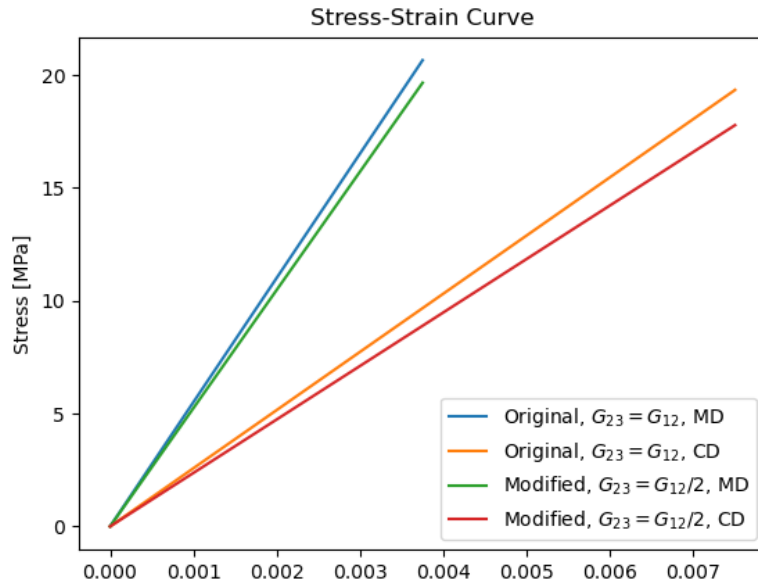
Figure 44: *Effects of shear modulus $G_{TT} = G_{23}$ on the reference volume in the elastic region*
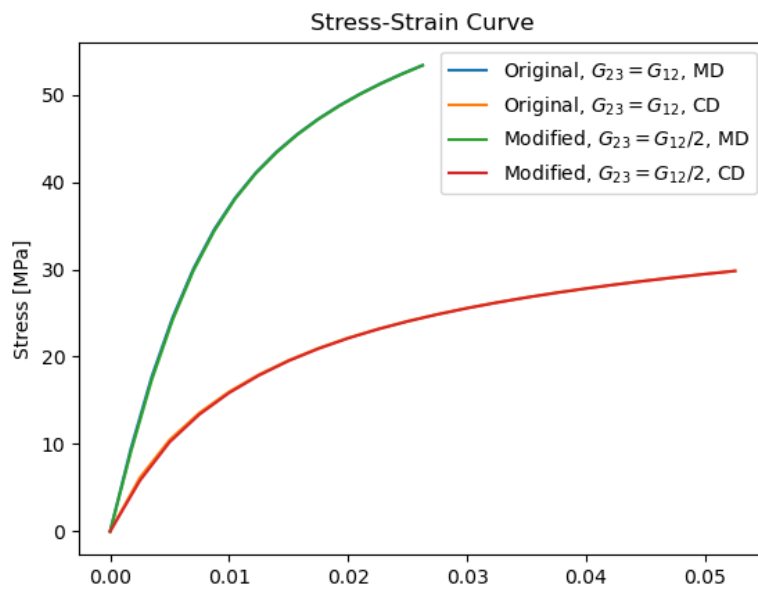

Figure 45: *Effects of shear modulus $G_{TT} = G_{23}$ on the reference volume in elasto-plastic region.*